Characteristics of transitional multicomponent gaseous and drop-laden mixing layers from direct numerical simulation: Composition effects

L. C. Selle
California Institute of Technology, Pasadena, California 91125

J. Bellan[a)]
California Institute of Technology, Pasadena, California 91125 and Jet Propulsion Laboratory, California Institute of Technology, Pasadena, California 91109-8099

(Received 13 November 2006; accepted 23 March 2007; published online 22 June 2007)

Transitional states are obtained by exercising a model of multicomponent-liquid (MC-liquid) drop evaporation in a three-dimensional mixing layer at larger Reynolds numbers, Re, than in a previous study. The gas phase is followed in an Eulerian frame and the multitude of drops is described in a Lagrangian frame. Complete dynamic and thermodynamic coupling between phases is included. The liquid composition, initially specified as a single-Gamma (SG) probability distribution function (PDF) depending on the molar mass, is allowed to evolve into a linear combination of two SGPDFs, called the double-Gamma PDF (DGPDF). The compositions of liquid and vapor emanating from the drops are calculated through four moments of their PDFs, which are drop-specific and location-specific, respectively. The mixing layer is initially excited to promote the double pairing of its four initial spanwise vortices, resulting into an ultimate vortex in which small scales proliferate. Simulations are performed for four liquids of different compositions, and the effects of the initial mass loading and initial free-stream gas temperature are explored. For reference, simulations are also performed for gaseous multicomponent mixing layers for which the effect of Re is investigated in the direct-numerical-simulation–accessible regime. The results encompass examination of the global layer characteristics, flow visualizations, and homogeneous-plane statistics at transition. Comparisons are performed with previous pretransitional MC-liquid simulations and with transitional single-component (SC) liquid-drop-laden mixing layer studies. Contrasting to pretransitional MC flows, the vorticity and drop organization depend on the initial gas temperature, this being due to drop/turbulence coupling. The vapor-composition mean molar mass and standard deviation distributions strongly correlate with the initial liquid-composition PDF. Unlike in pretransitional situations, regions of large composition standard deviation no longer necessarily coincide with those of large mean molar mass. The rotational and composition characteristics are all liquid-specific and the variation among liquids is amplified with increasing free-stream gas temperature. The classical energy cascade is found to be of similar strength, but the smallest scales contain orders of magnitude less energy than SC flows, which is confirmed by the larger viscous dissipation for MC flows. The kinetic energy and dissipation are liquid-specific and the variation among liquids is amplified with increasing free-stream gas temperature. The gas composition, of which the first four moments are calculated, is shown to be close to, but distinct from, a SGPDF. Eulerian and Lagrangian statistics of gas-phase quantities show that the different observation framework may affect the perception of the flow. © *2007 American Institute of Physics*.
[DOI: 10.1063/1.2734997]

I. INTRODUCTION

Sprays in combustion devices are used as the means to increase the surface area of the injected liquid and enhance evaporation and combustion. Virtually all fuels used in such practical devices are of petroleum type, being complex mixtures of hundreds to thousands of chemical species. While some of these species may be present in the liquid in minute concentrations, their importance may be totally disproportionate to their concentration with regard to ignition, pollution or deposition, and corrosion. Despite its relevance, the complete multicomponent aspect of the fuel, beyond the landmark binary-species model of Landis and Mills[1] that was adopted by many others (too many papers to be cited), has not received the well-deserved attention it merits until recently. Realizing the impossibility of accounting for each individual species as an element of a discrete set, which was the initial approach[1] adopted by many investigators, a statistical approach has recently been developed—a methodology that is much more attuned to large ensembles of variables. All MC-liquid statistical approaches have been based on continuous thermodynamics (CT) concepts. The CT theory[2,3] includes an appropriate representation of the chemical potential for a mixture containing numerous components and in-

[a)]Telephone: 1-818-354-6959. Fax: 1-818-393-6682. Electronic mail: josette.bellan@jpl.nasa.gov

volves a derivation of the Gibbs function through molecular thermodynamic methods in terms of the probability distribution function (PDF) describing the mixture composition. The concepts are fundamental and independent of the physicochemical model chosen for the chemical potential. From a specified initial composition PDF, the evolution of the mixture is determined by the physics of the situation encapsulated into thermodynamic relationships and/or conservation equations. Although the composition PDF generally depends on many variables, it can be tailored to depend on one or a restricted number of variables. For example, it was shown,[2,4–6] with validation, that the single-Gamma PDF (SGPDF) depending on the molar mass, m, can represent an entire homologous species class of hydrocarbons. Cotterman *et al.*[2] have used thermodynamic relations to show that during evaporation, the same mathematical form of the PDF applies in the gas phase as in the liquid from where the vapor originates. The flexibility of the CT approach in terms of the PDF mathematical form and of the choice of the PDF variable(s) makes it very attractive.

Tamim and Hallett[7] and Hallett[8] have pioneered the application of CT concepts to the study of a MC-liquid drop using a SGPDF. Their model has been adopted in practical simulations of spray combustors,[9] in Direct Numerical Simulation (DNS) of a transitional mixing layer having a lower stream initially laden with a large number [e.g., $O(10^6)$] of drops,[10] and even to atmospheric-science hydrocarbon-partitioning studies.[11] The SGPDF model has also constituted the point of departure for the development of models with an increasing range of application.[12–14] Specifically, Harstad *et al.*[14] have shown that the SGPDF model depending on m, while appropriate for slow evaporation in fuel-unvitiated surroundings, cannot describe even qualitatively evaporation under high-temperature or in fuel-vitiated conditions. Instead, a double-Gamma PDF (DGPDF) has been proposed, which when exercised for single drops compared excellently for most conditions with the results from a discrete-species model based on a 32-species representation. The flexibility of the statistical representation was manifested once more in the DGPDF model that was shown to fit all three preponderant homologous classes of Jet A, RP-1, and JP-7 petroleum fuels with only a single DGPDF when the PDF dependence is on $\sqrt{m}$ instead of on m.[13]

The recent pretransitional DGPDF DNS study of Le Clercq and Bellan[15] expanded on the previous SGPDF study of Le Clercq and Bellan[10] of the same mixing layer configuration: the DGPDF representation enables attainment of a higher evaporation regime, and thus the results have increased relevance to the realistic high-temperature regime of combustors. Both single component (SC) and SGPDF MC-liquid representations fail in such regime. Compared to previous studies,[10,15] the present DNS investigation accesses a higher-temperature turbulent-gas regime that is closer to that of real combustors, despite the fact that the initial gas temperature, T_0 (subscript 0 denotes the initial condition), is still very much lower than in combustors. This lower T_0 value is dictated by the requirement to match the drop characteristic time to that of the flow, which in this transitional regime is much larger than that of fully turbulent flows, known to be inaccessible in DNS. The focus of this study is on the effect of the drop/flow interaction, which exists only as long as the drop has not entirely evaporated. Thus, the interaction characteristic time is influenced by the liquid volatility, the initial drop size, the initial gas composition, the relative difference between T_0 and the initial drop temperature $T_{d,0}$, and the relative difference between $T_{d,0}$ and the liquid boiling temperature which for MC-liquid drops evolves with time as the liquid composition changes. To aid the unified understanding of MC turbulent flows, simulations are performed here both for single-phase (SP) MC flows, where the effect of the initial Reynolds number, Re_0, is investigated in the DNS-accessible regime, and for two-phase (TP) MC flows, where the effect of the initial mass loading, ML_0, and higher T_0 are explored with the same model.

This investigation is conducted within the framework of the DNS methodology wherein all scales of the flow are resolved. Originally devised for SP flows, DNS for TP flows with particles that are much smaller than the Kolmogorov scale and which have a volumetrically small loading ($\lesssim 10^{-3}$) was enabled by the results of Boivin *et al.*[16] showing that the drops can be treated as point sources of mass, momentum, and energy from the gas-phase perspective. It is thus appropriate to perform TP simulations using a gas-phase resolution that is adequate for SP flow by following the gas phase in an Eulerian frame and tracking the drops in a Lagrangian frame. The terminology DNS, while not strictly accurate, is traditionally applied to such simulations, and several recent studies have used this DNS methodology.[16–21]

This paper is organized as follows. In Sec. II, the conservation equations are briefly recalled from the detailed model developed by Le Clercq and Bellan.[15] Next, the configuration, boundary conditions, and the numerics are presented in Sec. III. Section IV is devoted to a description of the results, encompassing the global layer characteristics, flow visualizations, homogeneous-plane statistics, drop-ensemble probabilities, and a dissipation analysis. Comparisons with the SC DNS study of Okong'o and Bellan[20] and with the pretransitional DNS investigation of Le Clercq and Bellan[15] are also discussed. The results are summarized in Sec. V and future study directions are stated.

II. CONSERVATION EQUATIONS

The model of Ref. 15 is adopted wherein the MC liquid composition and gas composition in the vicinity of the drop surface are described by

$$P(m;\alpha_1,\beta_1,\alpha_2,\beta_2,\varepsilon) = (1-\varepsilon)f_\Gamma^{(1)} + \varepsilon f_\Gamma^{(2)}, \tag{1}$$

where $f_\Gamma^{(k)} = f_\Gamma(m;\alpha_k,\beta_k)$ with integer $k=1,2$, ε is a weighting parameter ($0 \leqslant \varepsilon \leqslant 1$), $\int_\gamma^\infty P(m)dm = 1$, and

$$f_\Gamma(m) = \frac{(m-\gamma)^{\alpha-1}}{\beta^\alpha \Gamma(\alpha)} \exp\left[-\left(\frac{m-\gamma}{\beta}\right)\right], \tag{2}$$

where $\Gamma(\alpha)$ is the Gamma function and $f_\Gamma(m)$ is a SGPDF. The origin of f is specified by γ [$P(m;\alpha_1,\beta_1,\alpha_2,\beta_2,\varepsilon)$ was developed in Ref. 14 with $\gamma_1=\gamma_2=\gamma$], and its shape is determined by α and β. At each time t, $P(m;\alpha_1,\beta_1,\alpha_2,\beta_2,\varepsilon)$ is determined by the vector $\eta \equiv (\alpha_1,\beta_1,\alpha_2,\beta_2,\varepsilon)$. According to

Harstad *et al.*,[14] P can be determined by an inverse mapping from its first four moments, ξ_n, where integer $n \in [1,4]$, with a fifth parameter empirically calculated. These moments are defined as

$$\xi_{nl} \equiv \int_{\gamma}^{\infty} m^n P_l(m)dm, \quad \xi_{nv} \equiv \int_{\gamma}^{\infty} m^n P_v(m)dm \tag{3}$$

for integer $n \geqslant 1$, where subscripts l and v denote the liquid and vapor, respectively. Although in the vicinity of each drop surface the vapor composition is represented by P_v according to Eq. (1), away from the drops the mathematical form of P_v is determined by the vapor released from the drops and by gaseous mixing. At each t, P_l describes the liquid-fuel composition, which is specific of each drop, and P_v describes the vapor composition, which varies with spatial location. Throughout this paper, we adopt the notation $\theta \equiv \xi_1$ and $\psi \equiv \xi_2$, and the standard deviation of P is calculated as $\sigma = \sqrt{(\psi - \theta^2)}$. Also following Ref. 14, one can define ξ_n^{SGPDF} as being the moments of a SGPDF that would have the same ξ_1 and ξ_2 values as a specified P. Thus, "excess moments" of any PDF P with respect to the SGPDF that has the same θ and ψ as P are defined by

$$\xi_n' \equiv \xi_n - \xi_n^{\mathrm{SGPDF}}. \tag{4}$$

By definition, $\xi_1' = \xi_2' = 0$ and a DGPDF then corresponds to $\xi_n' \neq 0$ for $n \geqslant 3$. Deviation of any PDF from the equivalent SGPDF decreases with decreasing $(\xi_n'/\xi_n^{\mathrm{SGPDF}})$.

A. Gas-phase equations

The gas is followed in an Eulerian frame, and the generic conservation equations for continuity, momentum, energy, species, and PDF first four moments $(\theta_v, \psi_v, \xi_{3v}, \xi_{4v})$ representing the composition are

$$\frac{\partial \Phi}{\partial t} + \frac{\partial [\Phi u_j]}{\partial x_j} = \frac{\partial [\Psi(\Phi)]}{\partial x_j} + S, \tag{5}$$

where

$$\Phi = \{c, cmu_i, cme_t, cX_v, cX_v\theta_v, cX_v\psi_v, cX_v\xi_{3v}, cX_v\xi_{4v}\} \tag{6}$$

is the vector of the conservative variables,

$$\Psi(\Phi) = \left\{ cm\mathcal{D}\frac{\partial}{\partial x_j}\left[\frac{X_v}{m}\left(1 - \frac{\theta_v}{m_a}\right)\right],\ -p\delta_{ij} + \sigma_{ij},\ -pu_j + u_i\sigma_{ij} + \lambda\frac{\partial T}{\partial x_j} + \alpha_1(T)\frac{\partial}{\partial x_j}\left(\frac{X_v}{m}\right) + \alpha_2(T)\frac{\partial}{\partial x_j}\left(\frac{X_v\theta_v}{m}\right) \right.$$
$$\left. + \alpha_3\frac{\partial}{\partial x_j}\left(\frac{X_v\psi_v}{m}\right),\ cm\mathcal{D}\frac{\partial}{\partial x_j}\left(\frac{X_v}{m}\right),\ cm\mathcal{D}\frac{\partial}{\partial x_j}\left(\frac{X_v\theta_v}{m}\right),\ cm\mathcal{D}\frac{\partial}{\partial x_j}\left(\frac{X_v\psi_v}{m}\right),\ cm\mathcal{D}\frac{\partial}{\partial x_j}\left(\frac{X_v\xi_{3v}}{m}\right),\ cm\mathcal{D}\frac{\partial}{\partial x_j}\left(\frac{X_v\xi_{4v}}{m}\right) \right\} \tag{7}$$

is the diffusional flux vector corresponding to Φ, and

$$S = \{S_{\mathrm{mole}}, S_{\mathrm{mom},i}, S_{\mathrm{en}}, S_{\mathrm{mole}}, S_{\mathrm{mass}}, S_{\psi}, S_{\xi_3}, S_{\xi_4}\} \tag{8}$$

is the source term vector of components S_r associated with Φ. In Eqs. (5)–(7), c is the molar density, x_i is the ith spatial coordinate, $\mathbf{u}$ is the mass-averaged velocity, X is the mole fraction, $m = \theta_v X_v + m_a(1 - X_v)$ is the molar mass, where m_a is the carrier gas molar mass (subscript a denotes the carrier gas), $\mathcal{D}$ is an effective diffusion coefficient defined by Harstad and Bellan[13] as the proportionality coefficient between the vapor mass flux and $cm\nabla(X_v/m)$, p is the pressure, σ_{ij} is the viscous stress tensor, δ_{ij} is the Kronecker symbol, $e_t = e_k + e_{int} = u_i u_i/2 + h - p/\rho$ is the total energy of the gas, $\rho = mc$ is the mass density, h is the enthalpy, λ is the thermal conductivity, and T is the gas temperature. The last three terms in the heat flux of the energy equation are the portion due to transport of species by the molar fluxes; the detailed expressions for $\alpha_1(T)$, $\alpha_2(T)$, and α_3 are presented in the Appendix. The source vector arises from the coupled interaction of drops and gas, and is presented in Sec. II C.

The perfect gas equation of state

$$p = (\rho R_u T)/m = cR_u T, \tag{9}$$

where R_u is the universal gas constant, closes the system of gas-phase equations.

B. Drop equations

Each drop is individually simulated and the liquid mass-density, ρ_l, is assumed constant although the liquid molar-density, c_l, may vary. Because $\rho/\rho_l = O(10^{-3})$, the gas phase is quasisteady with respect to the liquid phase,[22] and due to the relatively small value of T_0 compared to that in combustors, the evaporation rate is relatively low (verified in Le Clercq and Bellan[15]) so that the assumption of uniform internal drop properties is justified. The Lagrangian conservation equations for each drop position χ, velocity $\mathbf{v}$, energy, mass $M_d = V_d\rho_l = \pi\rho_l D^3/6$ (V and D represent volume and diameter, and the subscript d denotes the drop), and composition are

$$\frac{d\chi_i}{dt} = v_i, \quad \frac{dv_i}{dt} = \frac{F_i}{M_d}, \tag{10}$$

$$M_d C_l \frac{dT_d}{dt} = \underbrace{\frac{\lambda Nu}{D}\frac{\ln(1+B_T)}{B_T}A(T - T_d)}_{Q_{\mathrm{conv\text{-}diff}}} + \underbrace{\dot{m}_d\frac{L_{v\mathrm{eff}}}{B}}_{Q_{\mathrm{evap}}}, \tag{11}$$

$$\dot{m}_d \equiv \frac{dM_d}{dt} = -\frac{Sh}{3\mathrm{Sc}}\frac{M_d}{\tau_d}\ln(1+B), \tag{12}$$

$$\frac{d\xi_{nl}}{dt} = \frac{3\theta_l}{2BD^2}\frac{dD^2}{dt}\left\{\left[\frac{X_v}{m} - \frac{X_v^{(s)}}{m^{(s)}}(1+B)\right]\xi_{nl} + \frac{X_v^{(s)}\xi_{nv}^{(s)}}{m^{(s)}}(1+B) - \frac{X_v\xi_{nv}}{m}\right\} \tag{13}$$

for integer $n=[1,4]$, where the gas phase at the drop location, interpolated from the Eulerian solution, acts as the drop far field. $F_i=(M_d/\tau_d)f_1(u_i-v_i)$, where $\tau_d=\rho_l D^2/(18\mu)$ is the particle time constant for Stokes flow; T_d is the drop temperature; C_l is the liquid heat capacity at constant pressure; $A=\pi D^2$ is the drop-surface area; μ is the viscosity of the carrier gas; $\mathrm{Pr}=\mu C_p/(\lambda m)$, where C_p is the gas heat capacity at constant pressure, and $\mathrm{Sc}=\mu/(\rho\mathcal{D})$ are the Prandtl and the Schmidt numbers, respectively; and $\rho_l=c_l\theta_l$. The Nusselt, Nu, and the Sherwood, Sh, numbers are semiempirically modified using the Ranz-Marshall correlations, accounting for convective heat and mass transfer effects,[23] with the similarity assumption $\mathrm{Nu}=2+0.552\,\mathrm{Re}_{\mathrm{sl}}^{1/2}(\mathrm{Pr})^{1/3}$, $\mathrm{Sh}=2+0.552\,\mathrm{Re}_{\mathrm{sl}}^{1/2}(\mathrm{Sc})^{1/3}$. f_1, given in Miller and Bellan,[23]

$$f_1 = \frac{1+0.0545\,\mathrm{Re}_{\mathrm{sl}}+0.1\,\mathrm{Re}_{\mathrm{sl}}^{1/2}(1-0.03\,\mathrm{Re}_{\mathrm{sl}})}{1+a|\mathrm{Re}_b|^b}, \tag{14}$$

$$a = 0.09 + 0.077\exp(-0.4\,\mathrm{Re}_{\mathrm{sl}}),$$
$$b = 0.4 + 0.77\exp(-0.04\,\mathrm{Re}_{\mathrm{sl}}) \tag{15}$$

is an empirical correction to Stokes drag accounting for finite drop Reynolds numbers using the slip Reynolds number $\mathrm{Re}_{\mathrm{sl}}=|\mathbf{u}_{\mathrm{sl}}|\rho D/\mu$, where $\mathbf{u}_{\mathrm{sl}}=(\mathbf{u}-\mathbf{v})$ is the slip velocity, and for a Reynolds number $\mathrm{Re}_b=U_b\rho d/\mu$ based on the evaporation blowing velocity U_b obtained from the mass conservation relation at the drop surface, $\dot{m}_d=-\pi\rho D^2U_b$. The correlation of Eq. (14) is valid in the ranges $0\leqslant\mathrm{Re}_{\mathrm{sl}}\leqslant100$ and $0\leqslant\mathrm{Re}_b\leqslant10$. $B=(Y_v^{(s)}-Y_v)/(1-Y_v^{(s)})$ is the Spalding number, where $Y_v=X_v\theta_v/m$ is the vapor mass fraction, $Y_a=1-Y_v$, and $(1+B_T)=(1+B)^{1/\mathrm{Le}}$ with Le being the Lewis number, $L_{v\mathrm{eff}}$ is an effective latent heat[14] as defined in Appendix A of Le Clercq and Bellan,[15] and the superscript (s) denotes the drop surface. At this surface, the classical boundary conditions of temperature equality and mass, species, momentum, and energy flux conservation apply.[22] Under the ideal-mixture assumption, Raoult's law relates the drop and gas PDFs,

$$P_v^{(s)} = \frac{p_{\mathrm{atm}}}{X_v^{(s)}p}\exp\left[\frac{mL_v(m)}{R_uT_b(m)}\left(1-\frac{T_b(m)}{T_d}\right)\right]P_l^{(s)}, \tag{16}$$

where $p_{\mathrm{atm}}=1$ atm, and $L_v(m)$ and $T_b(m)$ are the latent heat and the normal boiling point, correlated as functions of m by Harstad *et al.*[14] using Trouton's law,

$$\Delta s_{\mathrm{lg}} = mL_v/T_b \simeq 10.6R_u, \tag{17}$$

and

$$T_b(m) = A_b + B_bm, \tag{18}$$

where $A_b=241.4$ and $B_b=1.45$ for T_b in K (see Appendix A of Le Clercq and Bellan[15] for more details).

Thus, the drops move throughout the flow according to the Lagrangian equations [Eqs. (10)] while heating [Eq. (11)], losing/gaining mass [Eq. (12)], and changing composition [Eq. (13)]. The thermodynamics at each drop surface, i.e., evaporation versus condensation for the species having molar mass m, is governed by Raoult's law, Eq. (16). That is, during its lifetime, each drop will encounter a gas-phase composition that is different from that which would have been expected had it remained in the gas resulting from its own evaporation, and it is this reality that produces the condensation of certain species onto the drop. No new drops are formed through homogeneous (Ref. 24) or heterogeneous nucleation.

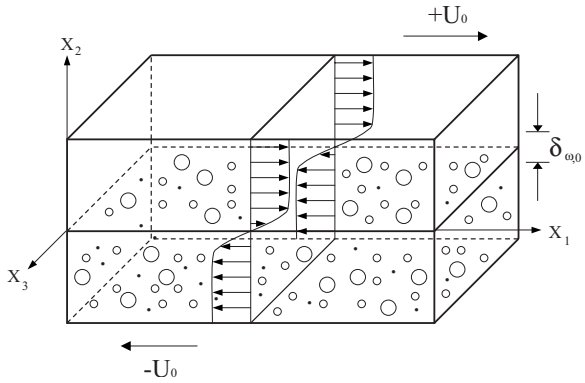

FIG. 1. Mixing layer configuration.

C. Source terms

The source-term-vector components of Eq. (8) are

$$S_r = -\sum_{q=1}^{N}\frac{w_q}{\Delta V_q}[\Lambda_r]_q, \tag{19}$$

$$\Lambda = \left\{\frac{d\mathcal{N}}{dt},\ F_j + \frac{d(\mathcal{N}\theta_l)}{dt}v_j,\ v_jF_j + Q_{\mathrm{conv-diff}} + Q_{\mathrm{evap}} + \dot{m}_d\left(\frac{v_jv_j}{2} + C_lT_d\right),\ \frac{d\mathcal{N}}{dt}, \frac{d(\mathcal{N}\theta_l)}{dt}, \frac{d(\mathcal{N}\psi_l)}{dt}, \frac{d(\mathcal{N}\xi_{3l})}{dt}, \frac{d(\mathcal{N}\xi_{4l})}{dt}\right\} \tag{20}$$

where $\mathcal{N}=M_d/\theta_l$ is the number of moles in the drop, N is the number of drops, and the summation in Eq. (19) is over all drops residing within a local numerical discretization volume, ΔV_q. Following previous methodology,[15,20,23] a geometric weighting factor w_q distributes the individual drop contributions to the nearest eight grid points in proportion to their distance from the drop location. Le Clercq and Bellan[10] explained that because convective effects dominate the species flux term, differential species diffusivity is negligible for MC flows in species transport from the drop location to the grid nodes.

III. CONFIGURATION, BOUNDARY AND INITIAL CONDITIONS, AND NUMERICS

The three-dimensional (3D) mixing layer configuration is displayed in Fig. 1, where the coordinates (x_1,x_2,x_3) cor-

TABLE I. Initial conditions. T_0 in K, ρ_l in kg/m^3, D_0 in m, and mean molar mass and standard deviation in kg/kmol. In all simulations, $M_{c,0}=0.35$, $\delta_{\omega,0}=6.859\times10^{-3}$m, $\{\{\mathrm{St}_0\}\}=3$, and $\{\{(\mathrm{St}_0-\{\{\mathrm{St}_0\}\})^2\}\}^{1/2}=0.5$, $T_{d,0}=345$ K, $X^u_{v,0}=10^{-4}$, $\gamma=86$ kg/kmol for diesel, $\gamma=41$ kg/kmol for Jet A, and $\gamma=93$ kg/kmol for RP-1 and JP-7. For $\mathrm{Re}_0=200$ the grid is $200\times224\times120$, for $\mathrm{Re}_0=500$ the grid is $360\times400\times216$, and for $\mathrm{Re}_0=600$ the grid is $432\times480\times260$. The baseline case is indicated by a superscript asterisk.

Case	Fuel	T_0	ML_0	ρ_l	Re_0	$X^l_{v,0}$	$\{\{D_0\}\}\times10^5$	$\theta_{l,0}/\sigma_{l,0}$	$\theta_{v,0}/\sigma_{v,0}$	$N_0\times10^{-3}$
die375ML0R5	Diesel	375	0	NA	500	$X^u_{v,0}$	NA	NA	140.0 / 28.0	NA
die375ML0R5X	Diesel	375	0	NA	500	10^{-1}	NA	NA	140.0 / 28.0	NA
die375ML0R6	Diesel	375	0	NA	600	$X^u_{v,0}$	NA	NA	140.0 / 28.0	NA
die375ML0R6X	Diesel	375	0	NA	600	10^{-1}	NA	NA	140.0 / 28.0	NA
die375ML2R2	Diesel	375	0.2	828	200	$X^u_{v,0}$	12.02	185.0 / 43.0	140.0 / 28.0	670
die400ML2R2	Diesel	400	0.2	828	200	$X^u_{v,0}$	11.64	185.0 / 43.0	140.0 / 28.0	690
die375ML2R5*	Diesel	375	0.2	828	500	$X^u_{v,0}$	7.601	185.0 / 43.0	140.0 / 28.0	2586
die375ML5R5	Diesel	375	0.5	828	500	$X^u_{v,0}$	7.601	185.0 / 43.0	140.0 / 28.0	6451
die400ML2R5	Diesel	400	0.2	828	500	$X^u_{v,0}$	7.359	185.0 / 43.0	140.0 / 28.0	2670
jetA375ML2R5	Jet A	375	0.2	800	500	$X^u_{v,0}$	7.732	161.0 / 29.7	131.4 / 22.4	2543
jetA400ML2R5	Jet A	400	0.2	800	500	$X^u_{v,0}$	7.487	161.0 / 29.7	131.4 / 22.4	2626
rp1375ML2R5	RP-1	375	0.2	800	500	$X^u_{v,0}$	7.732	165.2 / 17.7	153.5 / 14.8	2600
rp1400ML2R5	RP-1	400	0.2	800	500	$X^u_{v,0}$	7.487	165.2 / 17.7	153.5 / 14.8	2626
jp7375ML2R5	JP-7	375	0.2	800	500	$X^u_{v,0}$	7.732	167.1 / 19.2	153.7 / 15.7	2541
jp7400ML2R5	JP-7	400	0.2	800	500	$X^u_{v,0}$	7.487	167.1 / 19.2	153.7 / 15.7	2626

respond to the streamwise, cross-stream, and spanwise directions, respectively. The velocity difference across the layer is $\Delta U_0=2U_0$ and its mathematical form is prescribed using an error-function profile[23] having a width given by the initial vorticity thickness $\delta_{\omega,0}=\Delta U_0/\langle\partial u_1/\partial x_2\rangle$ [$\langle\rangle$ denotes averaging over homogeneous (x_1,x_3) planes]. A perturbation is imposed on the vorticity field to promote roll-up and pairing.[23,25,26] The forcing wavelengths in the x_1 and x_3 directions are l_1 and l_3, and their amplitudes with respect to the circulation are 10% and 2.25%, respectively. The evolution of the layer comprises two pairings of the four initial spanwise vortices to form an ultimate vortex in which small scales may proliferate if the Reynolds number is high enough. The dimensions of the domain are $L_1=4l_1(=29.16\delta_{\omega,0}=0.2$ m), $L_2=1.1L_1$, and $L_3=4l_3=0.6L_1$.

The gas-phase initial condition is specified by six parameters: T_0; the free-stream pressure p_0; $\mathrm{Re}_0=\rho_{a,0}\Delta U_0\delta_{\omega,0}/\mu$, where $\rho_{a,0}$ is the initial carrier gas (air) mass-density and μ is calculated from the specified value of Re_0; the Mach number $M_{c,0}$ based on the carrier gas initial speed of sound $a_{a,0}=\sqrt{R_aT_0C_{p,a}/C_{v,a}}$, where $R_a=R_u/m_a$ and the specific heats of the carrier ($C_{p,a}$ and $C_{v,a}$) are computed as in Ref. 27; the vapor molar fractions in the lower stream, $X^l_{v,0}$, and upper stream, $X^u_{v,0}$, here specified $X^l_{v,0}=X^u_{v,0}=10^{-4}$ for all TP simulations (this non-null value is realistic in that it simulates drop evaporation in vitiated air, as occurs in engines); and the specification of the free-stream vapor composition, which for each liquid is found from a single-drop simulation in air at the specified T_0 by choosing it to be the first-time-step surface-vapor composition. For SP simulations, either $X^l_{v,0}=X^u_{v,0}$, in which case there is no mass flux between streams, or $X^l_{v,0}=10^{-1}$ so as to create a vapor mass flux between the two streams; the value of 10^{-1} approximately corresponds to the average lower-stream value encountered at transitional states in TP simulations. The free-stream velocity $U_0=M_{c,0}a_{a,0}$ is calculated from the specified value of $M_{c,0}$. The thermal conductivity and diffusivity (both constant) are computed using the value of μ and specified values of Pr=Sc, 0.696 at $T_0=375$ K and 0.694 at $T_0=400$ K, calculated as in Ref. 27. The vapor heat capacity at constant pressure, $C_{p,v}$, is calculated as in Appendix A of Le Clercq and Bellan.[15] Table I lists all initial conditions and defines a baseline simulation; in addition to the $\mathrm{Re}_0=500$ and 600 simulations performed here, the table also lists some $\mathrm{Re}_0=200$ computation conditions of Le Clercq and Bellan,[15] as the present results will be compared to those of the listed pretransitional simulations. The initial mass loading, ML_0, defined as the ratio of the initial liquid mass to that of the gas in the lower stream, is null for SP simulations and $0<\mathrm{ML}_0<1$ for TP simulations. For TP computations, the $\mathrm{Re}_0=500$ simulations were close to the limit of the memory capacity of the computational platform (the $\mathrm{ML}_0=0.5$ simulation was almost at the memory limit), preventing TP simulations at higher Re_0.

In the TP simulations, only the lower stream of the mixing layer ($x_2<0$) is initially laden with drops, which are randomly distributed with a uniform number density and have at $t=0$ a null slip velocity with respect to the gas. The mean drop number density profile is smoothed near the centerline, $x_2=0$, using an error-function profile. The initial conditions for the drops are specified by $T_{d,0}$, which is uniform, with $T_{d,0}<T_0$ and a selected value of $(T_0-T_{d,0})$ to ensure that the drop/flow interaction is captured over the entire layer evolution with a substantial number of drops remaining in the simulation at all times (for the chosen $T_{d,0}=345$ K, these conditions were conservatively satisfied for all liquids when $T_0=375$ K and 400 K as shown in Sec. IV C); ML_0; the Stokes number St_0, where $\mathrm{St}\equiv\tau_d\Delta U_0/\delta_{\omega,0}$; ρ_l; and the liquid composition shown in Fig. 2, obtained through the selected-

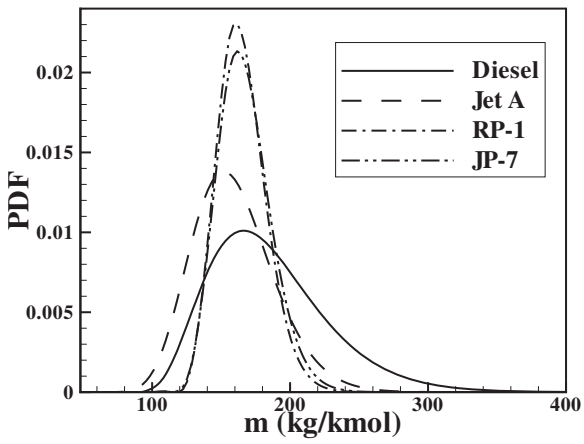

FIG. 2. Liquid initial PDF for each fuel.

PDF moments. Le Clercq and Bellan[15] emphasize that it is not possible to initialize all computations with the same values of the total number of drops, N_0, since ρ_l does not have the same value for all liquids and μ changes with T_0. Following the well accepted methodology of comparing simulations performed with specified nondimensional numbers rather than physical quantities,[28] the specification of ML_0 and St_0 determines for given ρ_l and T_0 the value of N_0 and D_0 (see Table I). The initial Stokes number is specified through a Gaussian distribution with mean $\{\{\mathrm{St}_0\}\}=3$ and standard deviation $\sqrt{\{\{\mathrm{St}_0^2\}\}-\{\{\mathrm{St}_0\}\}^2}=0.5$, where $\{\{\}\}$ symbolizes drop-ensemble averages over all drops. Similarly to the study of Le Clercq and Bellan,[15] four fuels are considered as practically significant examples of liquids, namely diesel, Jet A, RP-1 and JP-7, whose initial composition,[29] provided as a mole fraction versus the carbon number by Edwards,[30] was fitted in PDF form by Harstad and Bellan.[13] Table I lists the mean and standard deviation of the initial liquid PDF, $P_{l,0}$, which is assumed to be a SGPDF to enable the examination of the potential deviation from its initial SGPDF form.

The boundary conditions in the x_1 and x_3 directions are periodic, and adiabatic slip-wall conditions in the x_2 direction previously derived[31,32] were adapted by Le Clercq and Bellan[15] to the DGPDF CT model for MC mixtures (see Appendix B of Le Clercq and Bellan[15]). Drops reaching the slip walls are assumed to stick to them and are otherwise followed using the drop equations of Sec. II B.

The equations displayed in Sec. II A were solved using an eighth-order central finite-difference discretization in space and a fourth-order Runge-Kutta for temporal advancement. To mitigate potential numerical instabilities for long CPU time simulations, following Kennedy and Carpenter,[33] a tenth-order filtering for spatial derivatives was used (except in a half-filter-size band located at the lower and upper x_2 boundaries) at every time step. This filtering introduces a small amount of dissipation that serves only to stabilize the computations for long-time integrations, but since it acts only on the shortest waves that can be resolved on the grid, it does not act as a turbulence model and thus does not allow under-resolved computations (see Ref. 20). The time step was controlled by the CFL number. The grid size is listed in Table I and scales approximately linearly with Re_0.[34] The grid resolution is approximately 10^{-3} m, 0.55×10^{-3} m, and 0.46×10^{-3} m when $\mathrm{Re}_0=200$ (DNS of Ref. 15), 500, and 600, respectively. The $\sim10^{-3}$ value of $\{\{V_{d0}\}\}/\Delta V_q$ (computed using the values of $\{\{D_0\}\}$ in Table I) ensures that numerical diffusion induced by distributing the Lagrangian source terms at the Eulerian nodes is negligible. A fourth-order Lagrange interpolation, $\mathcal{I}$, was used to obtain gas-phase variable values at drop locations. Drops with a mass that decreased below 3% of the initial mass $M_{d,0}$ were removed from the calculation; for the conditions of this study, few drops fell below 3% of $M_{d,0}$ (at the two extremes are diesel simulations, where no drops disappeared, and RP-1 at $T_0=400$ K, where 9.8% of drops disappeared by transition) and mass was conserved in the system to a maximum relative error of 5×10^{-5}.

IV. RESULTS

A. Global layer evolution

1. Growth and dynamics

Figure 3 illustrates the global growth, mixing, and rotational characteristics of the layers. Growth is measured by the momentum thickness, δ_m,

$$\delta_m=\frac{\int_{x_2,\min}^{x_2,\max}[\langle\rho u_1\rangle_{x_2,\max}-\langle\rho u_1\rangle][\langle\rho u_1\rangle-\langle\rho u_1\rangle_{x_2,\min}]dx_2}{(\langle\rho u_1\rangle_{x_2,\max}-\langle\rho u_1\rangle_{x_2,\min})^2} \tag{21}$$

plotted versus $t^*\equiv t\Delta U_0/\delta_{\omega,0}$, where $x_{2,\max}=L_2/2$ and $x_{2,\min}=-L_2/2$ are the upper and lower boundaries of the computational domain. The overall variation of $\delta_m/\delta_{\omega,0}$ is typical of mixing layers with a roll-up region ($t^*<20$), and two regions of rapid increase ($20\leqslant t^*\leqslant 50$ and $65\leqslant t^*\leqslant 95$) each ending by a plateau corresponding to a pairing. Comparing simulations with different values of ML_0 in Fig. 3(a), $\delta_m/\delta_{\omega,0}$ peaks at $t^*=98$ for $\mathrm{ML}_0=0$ (unless otherwise stated, the $\mathrm{ML}_0=0$ simulations considered are those with $X^l_{v,0}=10^{-1}$ so as to approach as close as possible the $\mathrm{ML}_0\neq0$ simulations in terms of species mass transfer) independent of Re_0, at $t^*=103$ for all $\mathrm{ML}_0=0.2$ computations, and at $t^*=106$ for the $\mathrm{ML}_0=0.5$ simulation. The delay of the second pairing with increasing ML_0 is explained by the increasing total mass that must be entrained as the layer grows. For all $\mathrm{ML}_0=0.2$ computations shown in Fig. 3(b), $\delta_m/\delta_{\omega,0}$ peaks at $t^*=103$ showing independence of liquid composition; similarly, there seems to be independence of T_0 [Fig. 3(a) and information not shown]. The $\delta_m/\delta_{\omega,0}$ peak does not necessarily correspond to the transition time, t^*_{tr}, defined as that occurring when the energy spectra (discussed below) first exhibit classical turbulence characteristics. In Table II, t^*_{tr} and $\mathrm{Re}_{m,\mathrm{tr}}$ are listed where $\mathrm{Re}_m\equiv\mathrm{Re}_0\delta_m/\delta_{\omega,0}$. Tested only for SP computations, the value of $\mathrm{Re}_{m,\mathrm{tr}}$ increases nearly proportionally with Re_0. The $\mathrm{Re}_{m,\mathrm{tr}}$ value increases with ML_0 up to $\mathrm{ML}_0=0.2$, and decreases from $\mathrm{ML}_0=0.2$ to $\mathrm{ML}_0=0.5$, which was also found by Okong'o and Bellan[20] for SC-liquid drop-laden transitional mixing layers and was attributed to the initial

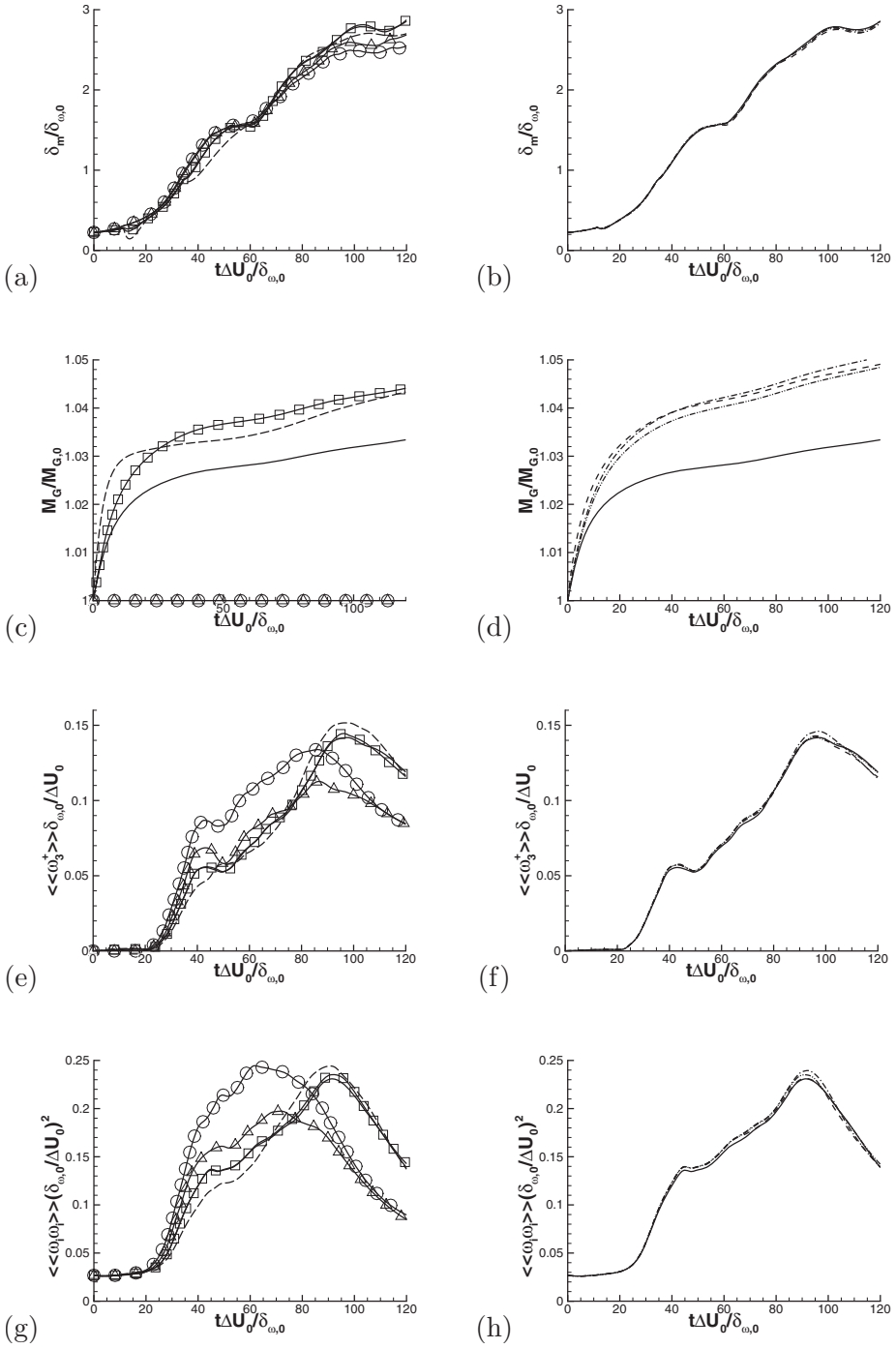

FIG. 3. Global layer characteristics: (a) $\delta_m/\delta_{\omega,0}$ for die375ML0R5 —△—, die375ML0R6 —○—, die375ML2R5 ——, die375ML5R5 — — — and die400ML2R5 —□—; (b) $\delta_m/\delta_{\omega,0}$ for die375ML2R5, jetA375ML2R5 – – –, rp1375ML2R5 – · – · – and jp7375ML2R5 – ·· – ·· –; (c) $M_G/M_{G,0}$ for all (a) simulations; (d) $M_G/M_{G,0}$ for all (b) simulations; (e) $\langle\langle\omega_3^+\rangle\rangle\delta_{\omega,0}/\Delta U_0$ for all (a) simulations; (f) $\langle\langle\omega_3^+\rangle\rangle\delta_{\omega,0}/\Delta U_0$ for all (b) simulations; (g) $\langle\langle\omega_i\omega_i\rangle\rangle(\delta_{\omega,0}/\Delta U_0)^2$ for all (a) simulations; (h) and (g) $\langle\langle\omega_i\omega_i\rangle\rangle \times(\delta_{\omega,0}/\Delta U_0)^2$ for all (b) simulations.

forcing that has a relatively weaker influence on the highest ML_0 value layers; that is, SP flows do not behave merely as a simple limit of TP flows. Although a small variation, at $T_0=375$ K the value of $Re_{m,tr}$ increases with increasing mean liquid molar mass, which is attributed to the decreased liquid volatility and consequently to the larger residual drop mass that promotes turbulence through drop/flow interactions. At $T_0=400$ K, the three kerosenes have similar $Re_{m,tr}$ values, which are distinctively smaller than that for diesel, showing that liquid-specificity effects increase with larger T_0. Therefore, the growth of the layer seems insensitive, but the global transitional characteristics seem mildly sensitive to the liquid identity.

The plot of $M_G/M_{G,0}$ in Figs. 3(c) and 3(d), where M_G is the gas-phase mass, gives a direct measure of global mass evolution. Expectably, no change in the initial amount of vapor occurs when $ML_0=0$, but either an increase in ML_0 or in T_0 results in an augmentation in $M_G/M_{G,0}$, as shown in Fig. 3(c). The major augmentation occurs before roll-up, after which $M_G/M_{G,0}$ increases more gradually and at generally similar rates for all diesel simulations, independent of ML_0 or T_0 values. However, the augmentation in $M_G/M_{G,0}$ occurs during the early time before roll-up for the larger ML_0 and during the late time before roll-up at the higher T_0, and is a much stronger function of T_0 than of ML_0. The strongest parameter influencing $M_G/M_{G,0}$ is the fuel composition, as

TABLE II. Global characteristics of simulations at transition. t^*_{tr} is the nondimensional time at transition and $Re_{m,tr}$ is the momentum-thickness based Reynolds number at transition. Except for the jetA375ML2R5 simulation, which was performed on a SGI Origin 2000 platform (on 64, R12000, 300 MHz processors), all other simulations were conducted on an Altix 3000 machine (on 32, Intel Itanium2, 900 MHz processors).

Case	CPU-hours	t^*_{tr}	$Re_{m,tr}$	CPU-hours at t^*_{tr}
die375ML0R5	793	120	1332	793
die375ML0R5X	1083	120	1343	1083
die375ML0R6	2260	110	1482	2072
die375ML0R6X	2802	110	1483	2568
die375ML2R5*	1680	100	1386	1400
die375ML5R5	2533	100	1336	2111
die400ML2R5	1706	100	1396	1422
jetA375ML2R5	9331	100	1365	7776
jetA400ML2R5	1700	100	1375	1417
rp1375ML2R5	1679	100	1377	1399
rp1400ML2R5	1694	100	1371	1412
jp7375ML2R5	1662	100	1381	1385
jp7400ML2R5	1701	100	1373	1417

depicted in Fig. 3(d). Compared to diesel, the more volatile kerosenes evaporate at a much larger rate during roll-up, and they continue to increase the vapor in the gas phase at a slightly higher rate than diesel even during the remaining layer evolution.

Figures 3(e)–3(h) display the rotational characteristics of the layer: the positive spanwise vorticity, $\langle\langle\omega_3^+\rangle\rangle\delta_{\omega,0}/\Delta U_0$, which is initially null and measures the small-scale activity, in Figs. 3(e) and 3(f), and the enstrophy, $\langle\langle\omega_i\omega_i\rangle\rangle \times(\delta_{\omega,0}/\Delta U_0)^2$, which is related to stretching and tilting and represents an important mechanism for turbulence production,[35] in Figs. 3(g) and 3(h); $\langle\langle\rangle\rangle$ denotes averaging over all grid points. The results show that the variation with Re_0 and ML_0 of both $\langle\langle\omega_3^+\rangle\rangle\delta_{\omega,0}/\Delta U_0$ and $\langle\langle\omega_i\omega_i\rangle\rangle \times(\delta_{\omega,0}/\Delta U_0)^2$ emulates the SC-liquid results discussed in detail by Okong'o and Bellan.[20] Up to the layer roll-up, corresponding to $t^* \approx 20$, the enstrophy displays little variation. Entrainment and pairing quickly produce enstrophy, and a steep increase in $\langle\langle\omega_i\omega_i\rangle\rangle(\delta_{\omega,0}/\Delta U_0)^2$ is observed that is more pronounced with larger Re_0 (a larger Re_0 naturally produces more flow distortion) and more subdued with increasing ML_0 (a larger ML_0 means that more mass must be entrained, which delays enstrophy production). As t^* increases, a small plateau in the magnitude of $\langle\langle\omega_i\omega_i\rangle\rangle(\delta_{\omega,0}/\Delta U_0)^2$ is encountered indicative of the first pairing, after which the enstrophy increases again and exhibits a peak at the second pairing. For $\langle\langle\omega_3^+\rangle\rangle\delta_{\omega,0}/\Delta U_0$, the time of the major peak seems independent of Re_0 for the SP layers; the peak is delayed with increasing ML_0 indicating the well-known stabilizing effect of small drops on a flow; and the value at the peak increases with Re_0 and ML_0, this being attributed to the enhanced small-scale formation at larger Reynolds numbers and the increased source of vorticity represented by a larger liquid mass (S_{mom} represents a source term in the vorticity equation), respectively. For all simulations, $\langle\langle\omega_i\omega_i\rangle\rangle \times(\delta_{\omega,0}/\Delta U_0)^2$ exhibits a peak earlier than $\langle\langle\omega_3^+\rangle\rangle\delta_{\omega,0}/\Delta U_0$, similar to the observations of Okong'o and Bellan.[20] Because the transitional time, t^*_{tr}, has similar values for all simulations (100 for all MC TP, 110 and 120 for SP $Re_0=500$ and 600), and given the peaking delay of TP with respect to SP simulations, the enstrophy at t^*_{tr} is reduced in SP cases with respect to TP ones. Variation of the enstrophy from its initial value is associated with the classical energy cascade that, unlike in two-dimensional flows, occurs in 3D flows,[35] and thus the $\langle\langle\omega_i\omega_i\rangle\rangle(\delta_{\omega,0}/\Delta U_0)^2$ relative magnitude with respect to the initial conditions is directly associated with the strength of the energy cascade. Viewed in this perspective, the fact that for the same initial conditions both SC SP and SC TP results of Okong'o and Bellan[20] [their Fig. 3(h)] display a similar magnitude $\langle\langle\omega_i\omega_i\rangle\rangle(\delta_{\omega,0}/\Delta U_0)^2$ peak to the corresponding MC SP and MC TP simulation means that the energy cascade is of similar strength for SC and MC flows. Whether for $\langle\langle\omega_3^+\rangle\rangle\delta_{\omega,0}/\Delta U_0$ in Figs. 3(e) and 3(f) or for $\langle\langle\omega_i\omega_i\rangle\rangle(\delta_{\omega,0}/\Delta U_0)^2$ in Figs. 3(g) and 3(h), T_0 and the liquid composition seem to have a negligible effect on the global rotational characteristics.

The peculiarities of energy transfer among scales in MC flows (of which the stretching and tilting activity represented by the enstrophy is only one manifestation) are embodied in the energy spectra depicted in Fig. 4 at t^*_{tr}. Both the streamwise spectra in Fig. 4(a) and the spanwise spectra in Fig. 4(b), shown as an example for u_1 and for selected simulations, exhibit a smooth behavior characteristic of turbulence [the peak observed in Fig. 4(b) is at the forcing frequency] and no accumulation of energy at the smallest scales, which indicates excellent spatial resolution. At the same Re_0, SP spectra have less energy in a given wavenumber than TP flows, which is attributed to their reduced vortical characteristics at t^*_{tr} [Fig. 3(a)]. The enhanced energy in the TP spectra is accentuated at the smallest wavenumber [Figs. 4(c) and 4(d), i.e., the decay rate is different in SP and TP cases], portraying the increased vortical features of TP flows at the small scales resulting from the source terms in the vorticity equation. The fact that at the smallest scale TP flows have more than two orders of magnitude more energy than SP flows is examined in more detail in Sec. IV D using higher-order measures. Increasing Re_0 produces a SP flow with an increased range of large wavenumbers, as expected, while increasing ML_0 increases the energy at the smaller wavenumbers and imperceptibly decreases the energy at the largest wavenumbers indicating a larger dissipation, a fact confirmed by the dissipation budget analysis of Sec. IV D. There is no sensitivity to T_0 and to the fuel composition. Compared to the TP SC results of Ref. 20, added to Fig. 4, the energy in the highest wavenumbers is reduced here by a factor of 10^5 in the streamwise direction [Fig. 4(c)] and by a factor of more than 10^4 in the spanwise direction [Fig. 4(d)] suggesting that because the energy cascade is of similar strength in SC and MC flows, the viscous dissipation must be larger in TP MC flows, which is confirmed in Sec. IV D. This drastic result has modeling implications in that subgrid-scale (SGS) models may (if transitional trends remain valid for fully developed turbulence) have relatively different importance in large eddy simulations (LES) of MC versus SC flows. Con-

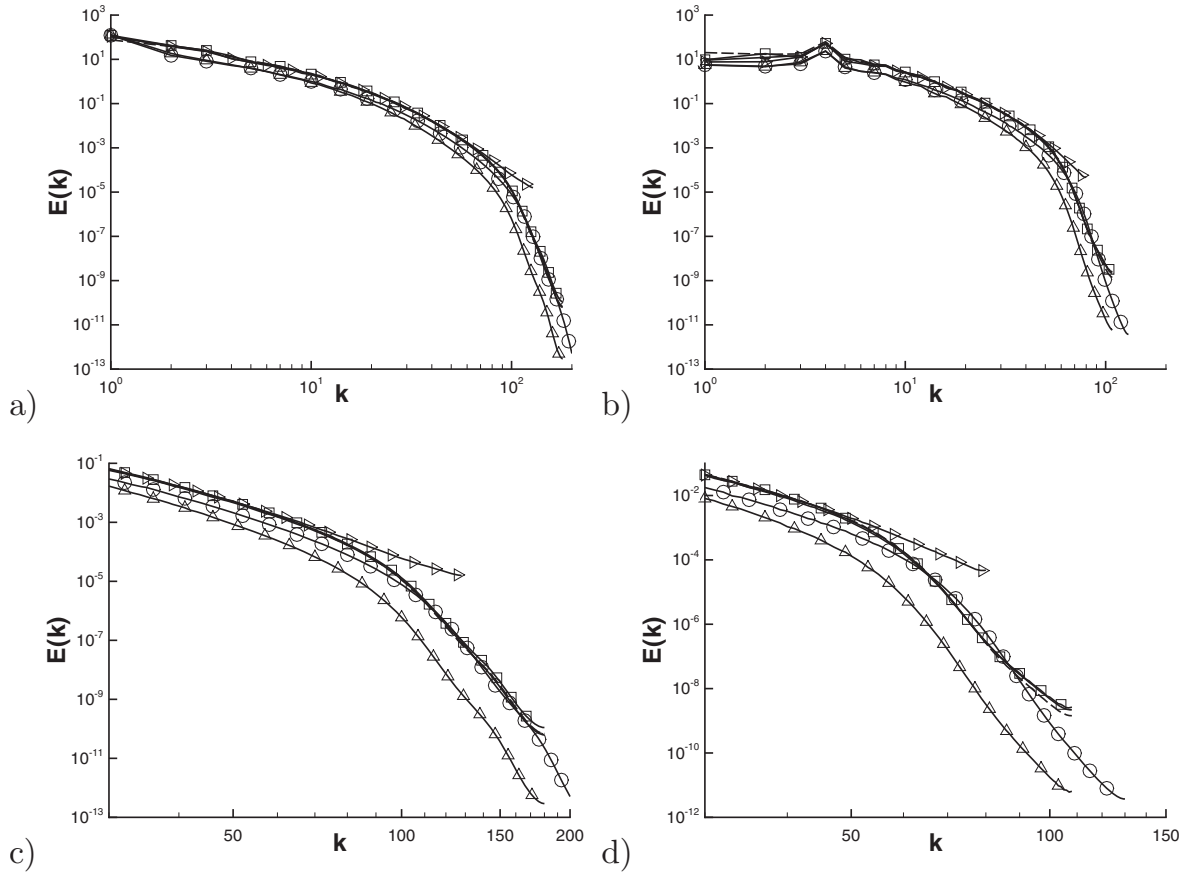

FIG. 4. One-dimensional u_1 energy spectra, at t_{tr}^* for die375ML0R5, die375ML0R6, die375ML2R5, die375ML5R5, and die400ML2R5: (a) full streamwise, (b) full spanwise, (c) streamwise zoom on the small scales, and (d) spanwise zoom on the small scales. The curve labels are listed in the Fig. 3 caption and –▷– denotes the n-decane results of Ref. 20 (added for comparison) at the same initial conditions.

sidering the lack of energy accumulation at the smallest scales in Fig. 4, confidence that the qualitative nature of the above results is independent of our grid size is provided by the grid resolution studies of Vreman,[36] in which simulations on three different grids provided the relevant flow properties within 2% deviation across grids for an Eulerian-Lagrangian model similar to ours.

The kinetic energy of the flow, $E_{kG}=\int_{\text{domain}}\rho(u_iu_i/2)dV$, illustrated in Fig. 5 as a fraction of its initial value, is insensitive to the Re_0 magnitude, while increasing ML_0 or T_0 promotes an initial augmentation of E_{kG}, and for ML_0 it eventually leads to a larger decay at t_{tr}^*, while for T_0 the opposite is observed. The different variation with ML_0 and T_0 is consistent in that in the former case the liquid mass fraction, ML, is larger with respect to the baseline case during the simulation, whereas in the latter case ML is smaller

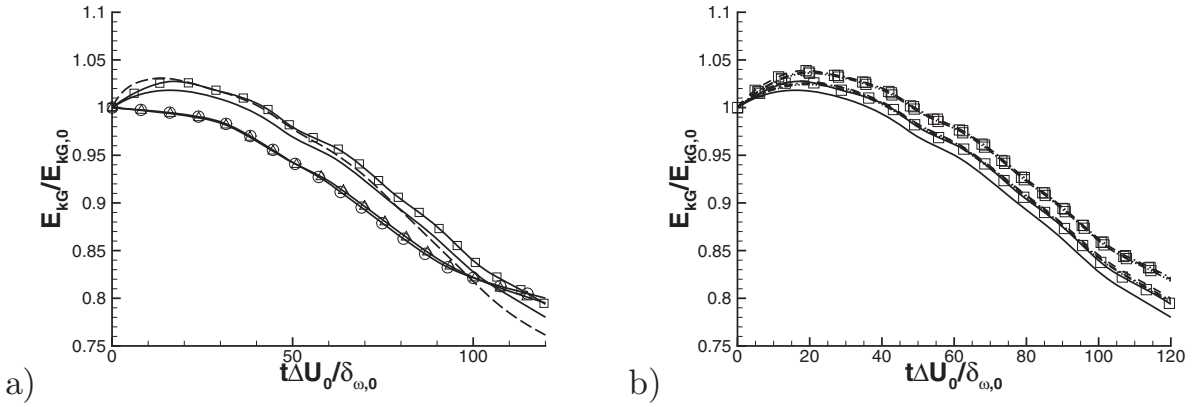

FIG. 5. Kinetic energy at t_{tr}^* normalized by the total initial gas energy (a) die375ML0R5, die375ML0R6, die375ML2R5, die375ML5R5, and die400ML2R5; (b) die375ML2R5, jetA375ML2R5, rp1375ML2R5, jp7375ML2R5, die400ML2R5, jetA400ML2R5, rp1400ML2R5, and jp7400ML2R5. The curve labels are listed in the Fig. 3 caption and additionally jetA400ML2R5 – □ –, rp1400ML2R5 – · □ – · □ – and jp7400ML2R5 – ·· □ – ·· □ –.

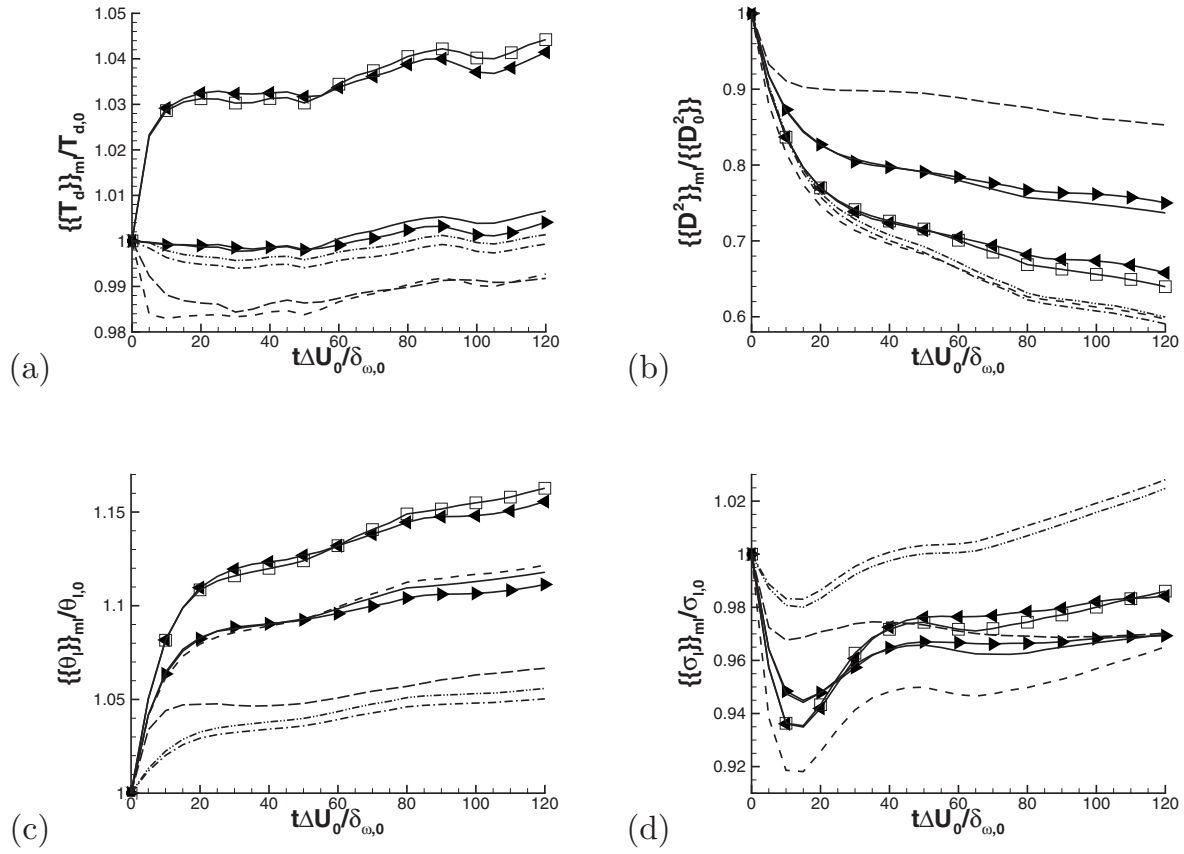

FIG. 6. Timewise evolution of drop characteristics ensemble-averaged in the mixing layer portion of the domain. Legend: die375ML2R2 —▶—, die400ML2R2 —◀—. Other curve labels are listed in the Fig. 3 caption.

due to the larger evaporation. Liquid composition effects shown in Fig. 5(b) are as strong as the ML_0 or T_0 effects. With increasing liquid volatility, $E_{kG}/E_{kG,0}$ increases, emulating the increased T_0 effect, and the rate of decay is slightly reduced, consistent with the dissipation budget discussed in Sec. IV D. At $T_0=375$ K the effect is small, and similar plots at $T_0=400$ K exhibit a slightly larger difference between liquids.

The results show that experiments conducted for MC model validation purposes, none of which currently exist, should not focus on global characteristics of the flow, with the exception of $M_G/M_{G,0}$, because they are not sensitive to the liquid composition.

2. Drop characteristics

Shown in Fig. 6 are mixing-layer Lagrangian ensemble averages portraying the evolution of the drop characteristics in that portion of the domain. The lower (upper) stream is defined as the region in which $\langle u_1\rangle \leqslant -0.99U_0$ ($\langle u_1\rangle \geqslant 0.99U_0$), and the mixing layer, which is the complement of the free-stream domain, is the region where $-0.99U_0 > \langle u_1\rangle > 0.99U_0$. Ensemble averages over the mixing layer are of interest here because it is that site which hosts most of the interaction between drops and a flow with turbulent characteristics; comparisons with the simulations of Le Clercq and Bellan[15] where the flow was pretransitional should reveal the effect of drop/turbulence interactions.

We define net evaporation as corresponding to a decrease in M_d, or equivalently $\dot{m}_d < 0$, or, since ρ_l is assumed constant, a decrease in D; net condensation corresponds to the reverse variation of these variables. Because of the multicomponent nature of the liquid, both net evaporation and net condensation may encompass concomitant evaporation of some species and condensation of other species. Figures 6(a) and 6(b) portray $\{\{T_d\}\}_{ml}/T_{d,0}$ and $\{\{D^2\}\}_{ml}/\{\{D_0^2\}\}$, where the subscript "ml" denotes the mixing layer. $\{\{T_d\}\}_{ml}/T_{d,0}$ varies only slightly, by at most a few % from $T_{d,0}$, and exhibits the undulatory behavior identified by Le Clercq and Bellan[10,15] to originate in the cooling and heating cycles experienced by the drops. Up to the first pairing, there is practically no difference between the present simulations and those of Le Clercq and Bellan,[15] however, past that station, $\{\{T_d\}\}_{ml}/T_{d,0}$ is larger here, which is a manifestation of the enhanced mixing due to turbulence that promotes drop heating. At the higher T_0, the drop heating is dominated between roll-up and first pairing by the total number of drops, resulting in a larger $\{\{T_d\}\}_{ml}/T_{d,0}$ for $Re_0=200$ (fewer drops), whereas past the first pairing the enhanced turbulent heating governs, leading to a larger $\{\{T_d\}\}_{ml}/T_{d,0}$ for $Re_0=500$. Jet A being the liquid containing the most volatile species, the corresponding drops experience the largest initial cooling resulting from the early evaporation, with further drop heating. RP-1 and JP-7, having relatively less volatile species than Jet A and narrow compositions, exhibit only modest cooling fol-

lowed by heating, and the slightly more volatile species in RP-1 lead to a slightly increased cooling with respect to JP-7. A larger ML_0 manifests in an enhanced drop cooling that rivals for diesel at $ML_0=0.5$ the cooling experienced by Jet A. For all liquids, however, the small variations in $\{\{T_d\}\}_{ml}/T_{d,0}$ translate in considerably larger variations in $\{\{D^2\}\}_{ml}/\{\{D_0^2\}\}$, with the rapid initial temperature change corresponding to the steepest decrease in the drop size, which subsides by the end of roll-up. An intermediary rate of evaporation follows that abates by the middle of the second pairing, upon reaching a very gradual drop reduction. The nonconstant rate of $\{\{D^2\}\}_{ml}/\{\{D_0^2\}\}$ decay is a mark of the ensemble averaging, as each individual drop obeys the classical D^2 law.[14] On going from pretransitional to transitional flow results, one notes an eventual reduction in $\{\{D^2\}\}_{ml}/\{\{D_0^2\}\}$ by ~5% (V_d by ~11%). Kerosene drops reach by the end of the simulation ~46% of $V_{d,0}$ compared to diesel's ~63%, and an increase in mass loading of a factor of 2.5 leads to a factor of ~1.7 increase in V_d by the end of the computation. Clearly, within the range of parameters investigated, the fuel identity is the most prominent factor influencing the drop size evolution.

Companion plots of $\{\{\theta_l\}\}_{ml}/\theta_{l,0}$ and $\{\{\sigma_l\}\}_{ml}/\sigma_{l,0}$ are displayed in Figs. 6(c) and 6(d). As in results portraying entire-domain ensemble averages from simulations of Le Clercq and Bellan,[15] the initial $\{\{\theta_l\}\}_{ml}/\theta_{l,0}$ surge is accompanied by a drastic reduction in $\{\{\sigma_l\}\}_{ml}/\sigma_{l,0}$ as the most volatile species evaporate, thus reducing the number of species in the drop. Eventually $\{\{\sigma_l\}\}_{ml}/\sigma_{l,0}$ reaches a minimum that coincides with a tapering off in the augmentation of $\{\{\theta_l\}\}_{ml}/\theta_{l,0}$. The interaction of drops with the flow promotes evaporation/condensation, and thus enhances changes in both $\{\{\theta_l\}\}_{ml}/\theta_{l,0}$ and $\{\{\sigma_l\}\}_{ml}/\sigma_{l,0}$. The augmentation in $\{\{\sigma_l\}\}_{ml}/\sigma_{l,0}$ indicates that condensation occurs, with a local plateau evident by the end of the first pairing; the concomitant increase in $\{\{\theta_l\}\}_{ml}/\theta_{l,0}$ indicates that, on an ensemble basis, evaporation is more effective than condensation in determining the mean liquid molar mass. Up to the first pairing there is no sensitivity to Re_0, however, once small scales become preponderant [Figs. 3(g) and 3(h)], one can detect not only quantitative but also qualitative differences between the pretransitional and transitional results; although $\{\{\theta_l\}\}_{ml}/\theta_{l,0}$ continues to increase in both cases, being larger in the latter situation, $\{\{\sigma_l\}\}_{ml}/\sigma_{l,0}$ for transitional computations reaches a minimum, then increases, and eventually crosses over the ever increasing $\{\{\sigma_l\}\}_{ml}/\sigma_{l,0}$ at $Re_0=200$. The decrease in $\{\{\sigma_l\}\}_{ml}/\sigma_{l,0}$ corresponds to a narrower DGPDF, and represents the accelerated release of species due to the drop/turbulence interaction. Eventually, the species evaporation becomes limited by the value of T_d while species condensation again augments $\{\{\sigma_l\}\}_{ml}/\sigma_{l,0}$. The lack of $\{\{\theta_l\}\}_{ml}/\theta_{l,0}$ and $\{\{\sigma_l\}\}_{ml}/\sigma_{l,0}$ variation in tandem as a function of Re_0 means that the pretransitional simulations do not merely represent an intermediary state to the transitional results because not only is the mean molar mass larger here, but the entire composition distribution is different due to the simultaneous evaporation and condensation of different species promoted by the turbulent flow transporting drops to various sites of the layer. For all liquids at the baseline conditions, $\{\{\theta_l\}\}_{ml}/\theta_{l,0}$ continuously increases with t^* as evaporation depletes increasingly less volatile species, but the rate of augmentation is not uniform even after the initial surge. This nonuniform rate is consistent with the nonmonotonic evolution of $\{\{\sigma_l\}\}_{ml}/\sigma_{l,0}$ representing evaporation when it decreases and condensation when it increases. At the larger ML_0, $\{\{\theta_l\}\}_{ml}/\theta_{l,0}$ no longer increases monotonically and instead experiences a minimum about halfway through the first pairing while $\{\{\sigma_l\}\}_{ml}/\sigma_{l,0}$ displays a maximum at the first pairing; that is, the reduction in T_d at the larger ML_0 results in decreasing evaporation, which, combined with the condensation of the lighter species, reduces the mean molar mass and further increases the width of the composition distribution. Clearly, as ML_0 increases, evaporation becomes governed by limitations in drop heating rather than by the drop/turbulence interaction. At the larger T_0, the larger (smaller) $\{\{\theta_l\}\}_{ml}/\theta_{l,0}$ for $Re_0=200$ than for $Re_0=500$ between roll-up and first pairing (after the first pairing) corresponds to the higher (lower) $\{\{T_d\}\}_{ml}/T_{d,0}$.

It is noteworthy that, except for the liquids with the narrowest composition PDF (i.e. RP-1 and JP-7), $\{\{\sigma_l\}\}_{ml}/\sigma_{l,0}$ does not exceed unity. That is, drops of liquids with a narrower composition are more prone to larger changes in the width of their composition distribution as each condensing species onto a drop makes a larger impact on the composition of the liquid drop. When the liquid composition has a PDF with a larger width, evaporation of species of ever decreasing volatility dominates the condensation of the lighter species within the time span of these simulations, resulting in a reduced composition heterogeneity.

Not surprisingly, the drop size and composition are good metrics to distinguish between various fuels and thus future experiments geared at model validation should strive to measure these quantities.

3. Vapor composition characteristics

The effect of Re_0 and ML_0 on the vapor composition is illustrated in Figs. 7(a) and 7(c), and the influence of liquid identity and T_0 is depicted in Figs. 7(b) and 7(d). Paralleling the drop ensemble averages of Fig. 6, the volumetric averages of Fig. 7 are also over the mixing layer portion of the domain. It is noteworthy that the simulation provides only the first four moments of the vapor composition, but not the mathematical form of its PDF. Indeed, consistent with the calculation of the source terms at grid nodes, the vapor-composition PDF is at each node the sum, according to Eq. (19), of all vapor PDFs at the drop surface for drops located within the grid volume associated with the specified node. The summation of DGPDFs having different values of same-order moments is not necessarily a DGPDF. Only the first two moments of the composition are examined in Fig. 7. The PDF representation of the vapor composition, including the higher moments, is addressed in Sec. IV E.

For diesel, independent of the initial conditions, $\langle\langle\theta_v\rangle\rangle_{ml}/\theta_{v,0}$ experiences a sustained growth from unity, initially representing the combined effect of condensation of lighter species onto drops, as is obvious from the sharp decay in $\langle\langle\sigma_v\rangle\rangle_{ml}/\sigma_{v,0}$, and of species heavier than $\theta_{v,0}$ that may

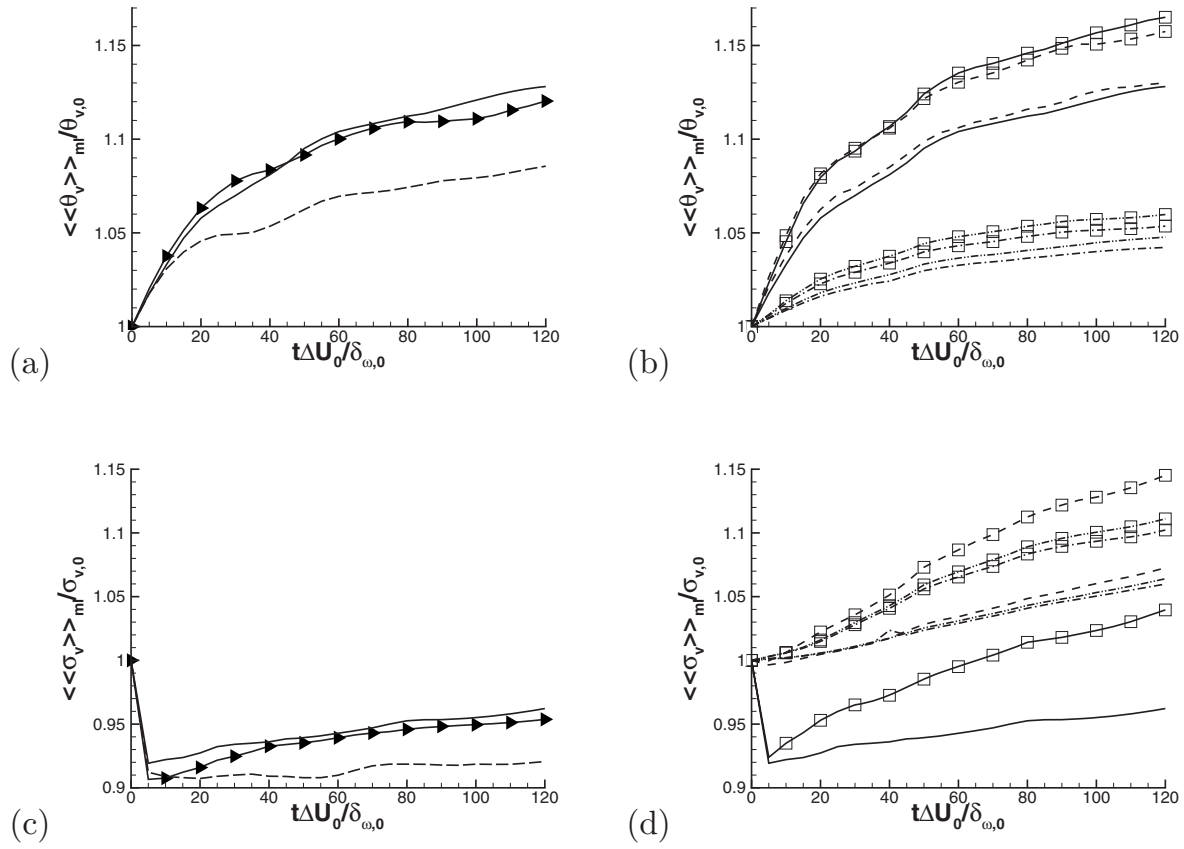

FIG. 7. Timewise evolution of domain-averaged gas characteristics in the mixing layer. [(a) and (c)] die375ML2R2, die375ML2R5, and die375ML5R5; and [(b) and (d)] die375ML2R5, die400ML2R5, jetA375ML2R5, jetA400ML2R5, rp1375ML2R5, rp1400ML2R5, jp7375ML2R5, and jp7400ML2R5. Curve labels are listed in the Figs. 3, 6, and 5 captions.

have been released through drop evaporation. Further increase in $\langle\langle\theta_v\rangle\rangle_{\mathrm{ml}}/\theta_{v,0}$ is accompanied by an augmentation in $\langle\langle\sigma_v\rangle\rangle_{\mathrm{ml}}/\sigma_{v,0}$, showing that although evaporation of some species occurs concomitantly with condensation of other species, during the remainder of the simulation it is species addition from the liquid phase that dominates the changes in the vapor composition. In contrast, the kerosenes experience an immediate increase in $\langle\langle\theta_v\rangle\rangle_{\mathrm{ml}}/\theta_{v,0}$ due to evaporation, as $\langle\langle\sigma_v\rangle\rangle_{\mathrm{ml}}/\sigma_{v,0}$ simultaneously increases. Compared to a change in Re_0 by a factor of 2.5, a change by the same factor in ML_0 produces a much larger effect on $\langle\langle\theta_v\rangle\rangle_{\mathrm{ml}}/\theta_{v,0}$ and $\langle\langle\sigma_v\rangle\rangle_{\mathrm{ml}}/\sigma_{v,0}$. The much reduced $\langle\langle\theta_v\rangle\rangle_{\mathrm{ml}}/\theta_{v,0}$ obtained when $\mathrm{ML}_0=0.5$ results from the increased condensation detected in Fig. 7(c), reflecting drop-heating relative impediments, and is consistent with the lower $\{\{T_d\}\}_{\mathrm{ml}}/T_{d,0}$ in Fig. 6(a). The larger initial decay experienced by $\langle\langle\sigma_v\rangle\rangle_{\mathrm{ml}}/\sigma_{v,0}$ at the lower Re_0 [Fig. 7(c)] shows that relative to the higher Re_0, a larger number of species condenses and because the condensing species have a smaller molar mass, this process produces a higher $\langle\langle\theta_v\rangle\rangle_{\mathrm{ml}}/\theta_{v,0}$ from roll-up to the first pairing [Fig. 7(a)]. Past the first pairing, the larger $\{\{T_d\}\}_{\mathrm{ml}}/T_{d,0}$ at the higher Re_0 [Fig. 6(a)] leads to increasing evaporation versus condensation which augments $\langle\langle\sigma_v\rangle\rangle_{\mathrm{ml}}/\sigma_{v,0}$ and elevates $\langle\langle\theta_v\rangle\rangle_{\mathrm{ml}}/\theta_{v,0}$ through the addition of higher molar mass species.

Mirroring the drop composition characteristics, changes in the vapor composition are smallest for the narrowest composition-PDF kerosenes for which the vapor mean molar mass increases [Fig. 7(b)] owing to net evaporation [Fig. 7(d)]; T_0 has only a very modest effect as the species thermodynamics are quite similar for the narrow compositions. Although initial net evaporation also increases $\langle\langle\theta_v\rangle\rangle_{\mathrm{ml}}/\theta_{v,0}$ for Jet A, its much wider composition PDF leads to a correspondingly greater T_0 impact. Finally, as already discussed, diesel is distinct from all other liquids in that the augmentation of $\langle\langle\theta_v\rangle\rangle_{\mathrm{ml}}/\theta_{v,0}$ is initially due to condensation of lighter vapor species onto the drops and also to evaporation of heavier species from the drops, and its much wider composition PDF makes it prone to the largest influence of T_0.

It is noteworthy that the value of $\langle\langle\theta_v\rangle\rangle/\theta_{v,0}$ has a theoretical maximum limit corresponding to complete drop evaporation. Neglecting the initial amount of vapor (which here represents less than 0.53% of the total liquid mass), if all liquid were evaporated, the composition of the vapor would be that of the liquid at $t^*=0$, that is, $\max(\langle\langle\theta_v\rangle\rangle/\theta_{v,0})=\theta_{l,0}/\theta_{v,0}$. From Table I one finds that $\theta_{l,0}/\theta_{v,0}$ is 1.32 for diesel, 1.23 for Jet A, 1.076 for RP-1, and 1.087 for JP-7. The departure of $\langle\langle\theta_v\rangle\rangle/\theta_{v,0}$ from these asymptotic limits depends on the amount of vapor already released. The impact of T_0 is only on the evaporation rate,

and thus on the time needed to reach this asymptotic value. Consequently, the bunching in Fig. 7(b) of $\langle\langle\theta_v\rangle\rangle/\theta_{v,0}$ for RP-1 and JP-7 is consistent with their similar values of $\theta_{l,0}/\theta_{v,0}$ and evaporation rates [Fig. 6(b)], and curves for Jet A and diesel match by happenstance as a result of the competing effects between the significantly higher asymptotic limit for diesel and the much higher evaporation rate for Jet A [Fig. 6(b)]. These considerations are independent of the actual composition of the initial vapor; however, because the initial vapor is found here from a single-drop simulation in air at the specified T_0 (by choosing it to be the first-time-step surface-vapor composition), this means that $\theta_{v,0}$ depends on $\theta_{l,0}$ through the width of the liquid-PDF, finally explaining why RP-1 and JP-7 on the one hand and diesel and Jet A on the other hand show similar $\langle\langle\theta_v\rangle\rangle/\theta_{v,0}$.

Clearly, averaged quantities can only give a general physical picture of the flow, and detailed visualizations, presented next, are necessary to understand the details of the situation.

B. Flow visualizations

1. Drop field

The detailed distribution of the drop number density, ρ_n, calculated as an Eulerian field from the Lagrangian distribution

$$\rho_n = \sum_{q=1}^{N_d} \frac{w_q}{\Delta V_q} \tag{22}$$

is presented in Fig. 8. The plots depict the between-the-braid plane $x_3/L_3=0.5$ for selected simulations, each at t_{tr}^*. All simulations display an intricate drop organization exhibiting a multitude of scales. The void regions correspond to locations of high vorticity[37] and contain no drops as the ρ_n value based on one drop per computational volume leads to $\rho_n = 5.9\times10^9$ m^{-3}. The outline of the void regions corresponds to high-strain locations (Ref. 37; also see Sec. IV C 1) and displays large concentrations of drops.

Increasing ML_0 [Figs. 8(a) and 8(c)] leads to a more intricate drop organization exhibiting a larger range of scales; this is because at the same St_0 value, the larger N_0 induces more drop/flow interaction, which amplifies local nonuniformities through the drag action. The larger ML_0 leads expectably to higher ρ_n values.

With increasing T_0, diesel [Figs. 8(a) and 8(b)] and JP-7 [Figs. 8(g) and 8(h)] exhibit more heterogeneity in the lower stream and part of the mixing layer, with void regions that now punctuate the rather uniform ρ_n lower stream. These new regions of small ρ_n result from the enhanced drop heating, which promotes evaporation. No such regions are detected for Jet A [Figs. 8(e) and 8(f)] within the range of displayed ρ_n, although structural changes with increasing T_0 are clearly visible. This dependency of the drop organization on T_0 should be contrasted with the insensitivity to T_0 found in the pretransitional simulations of Le Clercq and Bellan.[15] It is thus clear that the coupling between turbulence and drops creates this T_0 dependency.

Composition effects, examined at both $T_0=375$ K [Figs. 8(a), 8(e), and 8(g)] and 400 K [Figs. 8(b), 8(d), 8(e), and 8(h)], show that the complexity of the drop organization decreases with increased fuel volatility, indicating that by reducing the drop size and thus the local drop/flow drag force, early evaporation has a homogenizing effect on the ρ_n structure. Because at $T_0=400$ K all kerosenes have the same N_0 and $\{\{D_0\}\}$ (see Table I), the different ρ_n distributions portrayed in Figs. 8(b), 8(d), 8(e), and 8(h) result solely from the different liquid composition. The global structural organization for RP-1 and JP-7 (which have similar composition PDFs) at the same initial conditions is virtually identical, although local differences in the structure of the field and value of ρ_n are visible.

Additional insight into the relationship between the drop position, its temperature, and its composition is achieved by examining Lagrangian visualizations displayed in Fig. 9 for the baseline case at t_{tr}^* in the mixing layer portion of the domain; each sphere in the plot represents a physical drop, the drops are magnified for readability, and there is no relationship between a drop size and its plotted volume. Due to the viewing angle, the void regions evident in Fig. 8 are obscured. The lower part of the mixing layer is populated by low-T_d drops [Fig. 9(a)], but as the drops penetrate further into the mixing layer, they heat up and form temperature-wise a very heterogeneous drop ensemble. The largest T_d is achieved by drops located at the top of the ultimate vortex, as they are in contact with the upper stream carrier gas at T_0. The impact of T_d on θ_l is evident in Fig. 9(b). Both the drop history and its instantaneous T_d determine the value of θ_l, as not all drops within a given temperature range have the same composition. The drops with the smallest θ_l are located in the lower part of the mixing layer, and their θ_l is noticeably higher than $\theta_{l,0}$ owing to the already evaporated volatiles. The mixing layer contains drops with a great variety of compositions and the composition diversity is also obvious in the remnant of the initial four spanwise vortices; a quantitative measure of the heterogeneous distribution is presented in Sec. IV C 1. Drops having $\theta_l>245$ kg/kmol are primarily located at the top of the ultimate vortex. However, not all drops at that location have $\theta_l>245$ kg/kmol, as most drops there have $235\ \mathrm{kg/kmol}<\theta_l<245\ \mathrm{kg/kmol}$. Moreover, some drops with $235\ \mathrm{kg/kmol}<\theta_l<245\ \mathrm{kg/kmol}$ are also found embedded deep in the lower part of the ultimate vortex. This substantial local variation in θ_l is premonitory of what could be expected for θ_v.

2. Flow field

a. Dynamics. To differentiate between SP and TP simulations, the between-the-braid plane $\omega_3\delta_{\omega,0}/\Delta U_0$ is first displayed in Fig. 10 for all $\mathrm{ML}_0=0$ computations. In all cases, the complex structure of the flow is apparent with regions of negative values, as in the initial condition, interspersed with regions of substantial positive values that are a manifestation of the developed small-scale activity. The maximum $\omega_3\delta_{\omega,0}/\Delta U_0$ value increases with Re_0, as expected, and decreases with increasing $(X_{v,0}^l - X_{v,0}^u)$, which is attributed to the correspondingly increasing scalar dissipation, a fact confirmed in Sec. IV D. The increased scalar dissipation contrib-

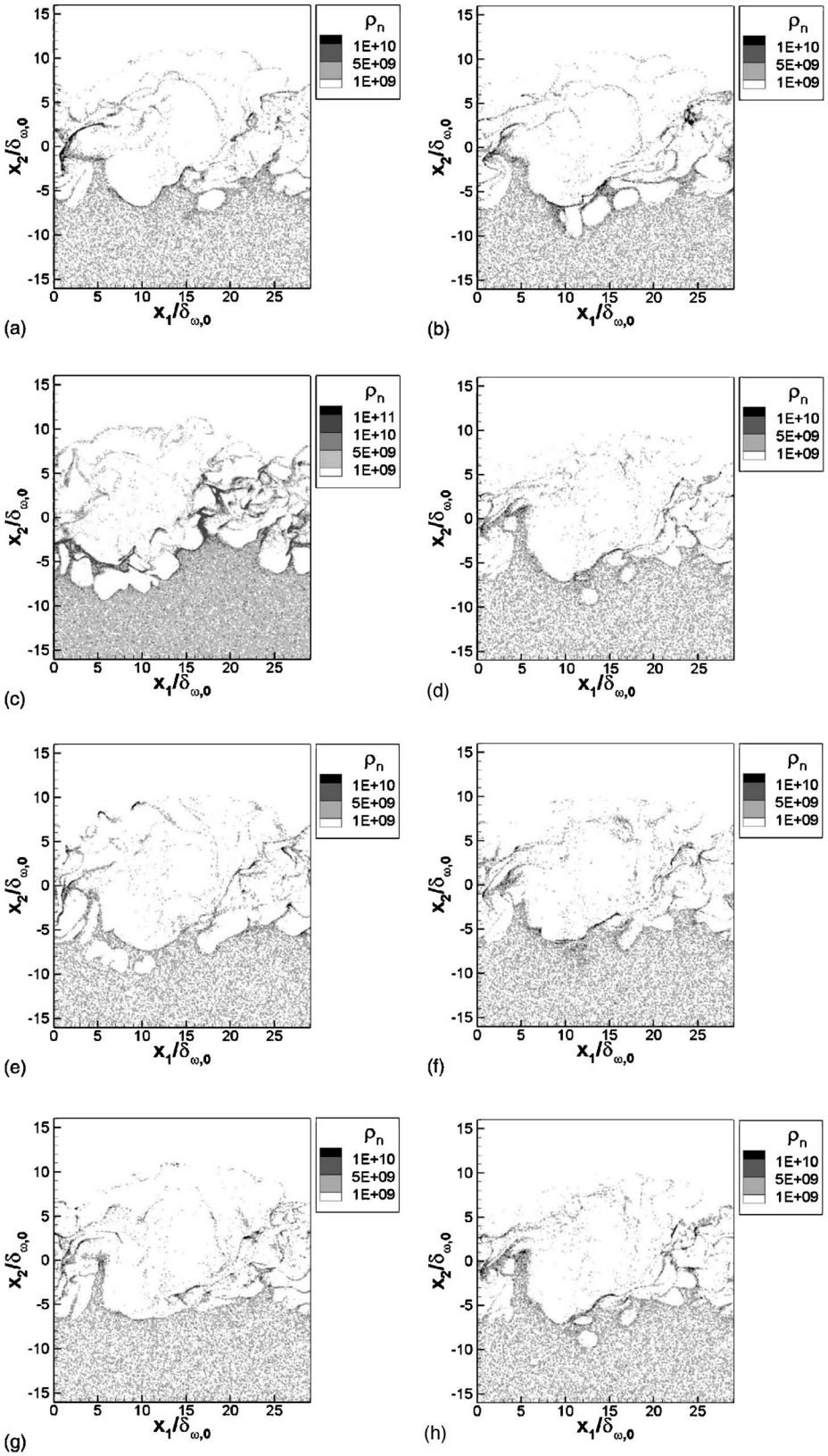

FIG. 8. Drop number density (m^{-3}) in the between-the-braid plane ($x_3/L_3=0.5$) at t_{tr}^*: (a) die375ML2R5, (b) die400ML2R5, (c) die375ML5R5, (d) rp1400ML2R5, (e) jetA375ML2R5, (f) jetA400ML2R5, (g) jp7375ML2R5, and (h) jp7400ML2R5.

utes to the larger dissipation, and due to the coupling of the dynamics with scalar transport, the viscous dissipation whose role is the reduction of organized motion also increases (Sec. IV D), which decreases the vorticity.

The $ML_0 \neq 0$ spanwise vorticity is illustrated in Fig. 11 for the same simulations shown in Fig. 8. The maximum $\omega_3 \delta_{\omega,0}/\Delta U_0$ value increases with increasing ML_0 when going from null to non-null values [compare with Fig. 10(a)] but the opposite occurs when ML_0 changes from 0.2 to 0.5, and instead concentrated regions of high vorticity appear,

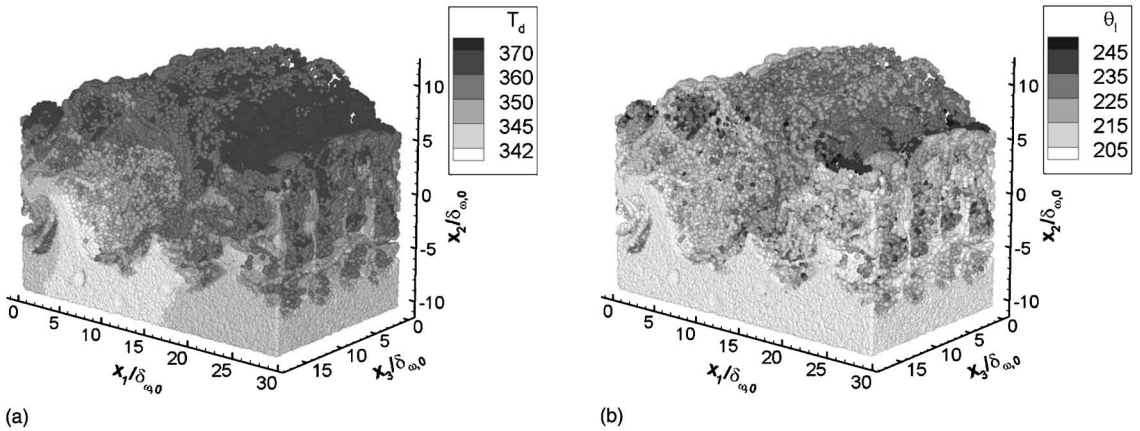

FIG. 9. Lagrangian plot of all drops at t_{tr}^{*} for die375ML2R5. (a) T_d and (b) θ_l. The drops are magnified and their volume is not proportional to their size.

conjectured to result from the amplified local interaction of the larger size drops [Fig. 6(b)] with the flow. The value of T_0 has considerably more impact than ML_0 in determining the $\omega_3\delta_{\omega,0}/\Delta U_0$ activity and its maximum value. Although for diesel, JP-7, and RP-1 the larger T_0 increases the maximum $\omega_3\delta_{\omega,0}/\Delta U_0$, the opposite occurs for Jet A. This liquid-specific behavior is explained by the variation of the source magnitude, $\nabla\times(\mathbf{S}_{\text{mom}}/\rho)=\nabla\times\{(1/\rho)[\mathbf{F}+(d(\mathcal{N}\theta_l)/dt)\mathbf{v}]\}$, in the vorticity equation. Evidently, this source contains two terms: the drag, which has on average positive components, the magnitude of which decreases with the decreasing drop size promoted by the increasing T_0, and the momentum of the vapor released from the drops, which has on average negative components, the magnitude of which increases in absolute value with increasing T_0. In the ω_3 equation, this term is $((\partial(S_{\text{mom},1}/\rho)/\partial x_2)-(\partial(S_{\text{mom},2}/\rho)/\partial x_1))$, meaning that

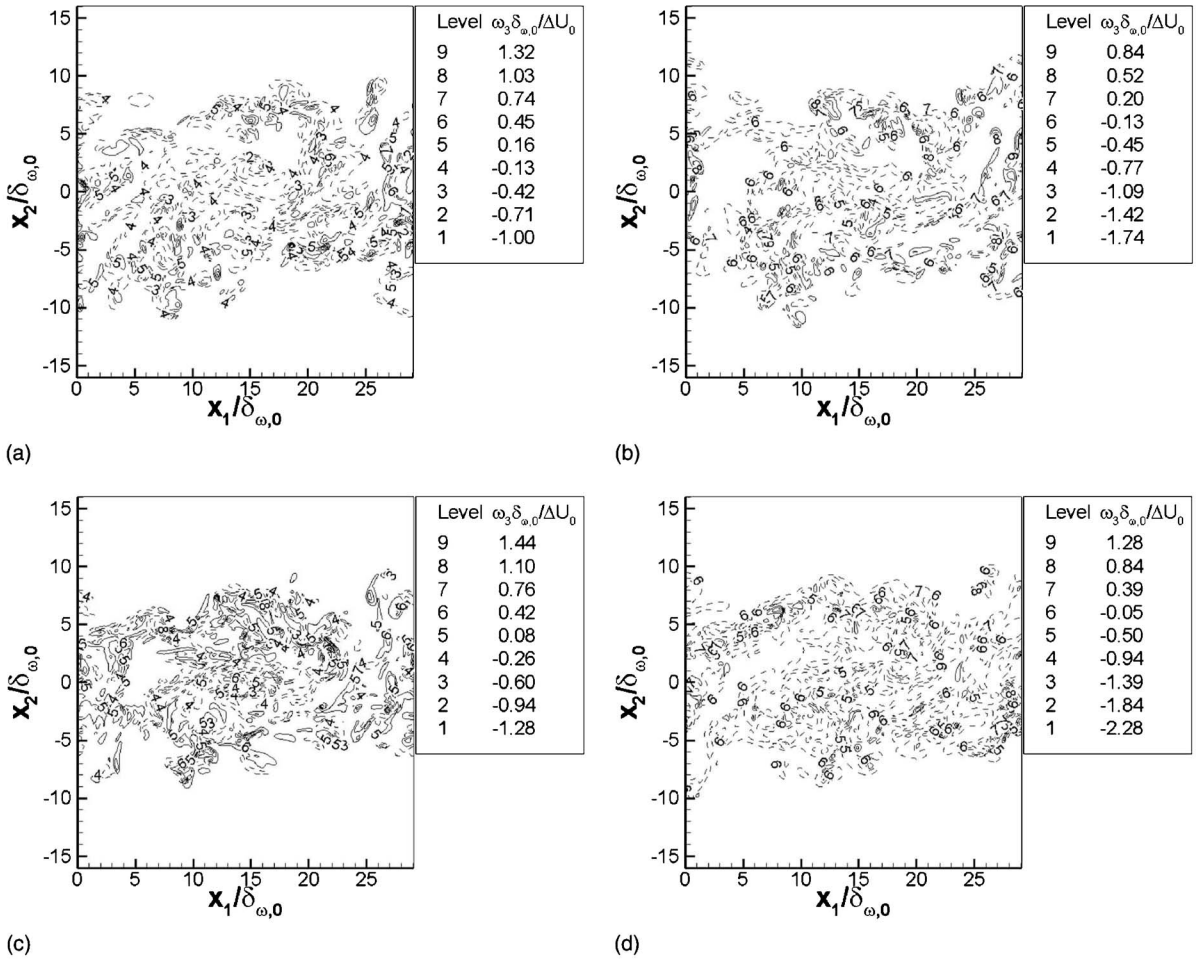

FIG. 10. Spanwise vorticity in the between-the-braid plane ($x_3/L_3=0.5$) at t_{tr}^{*}: (a) die375ML0R5, (b) die375ML0R5X, (c) die375ML0R6, and (d) die375ML0R6X. Dashed lines represent negative vorticity values.

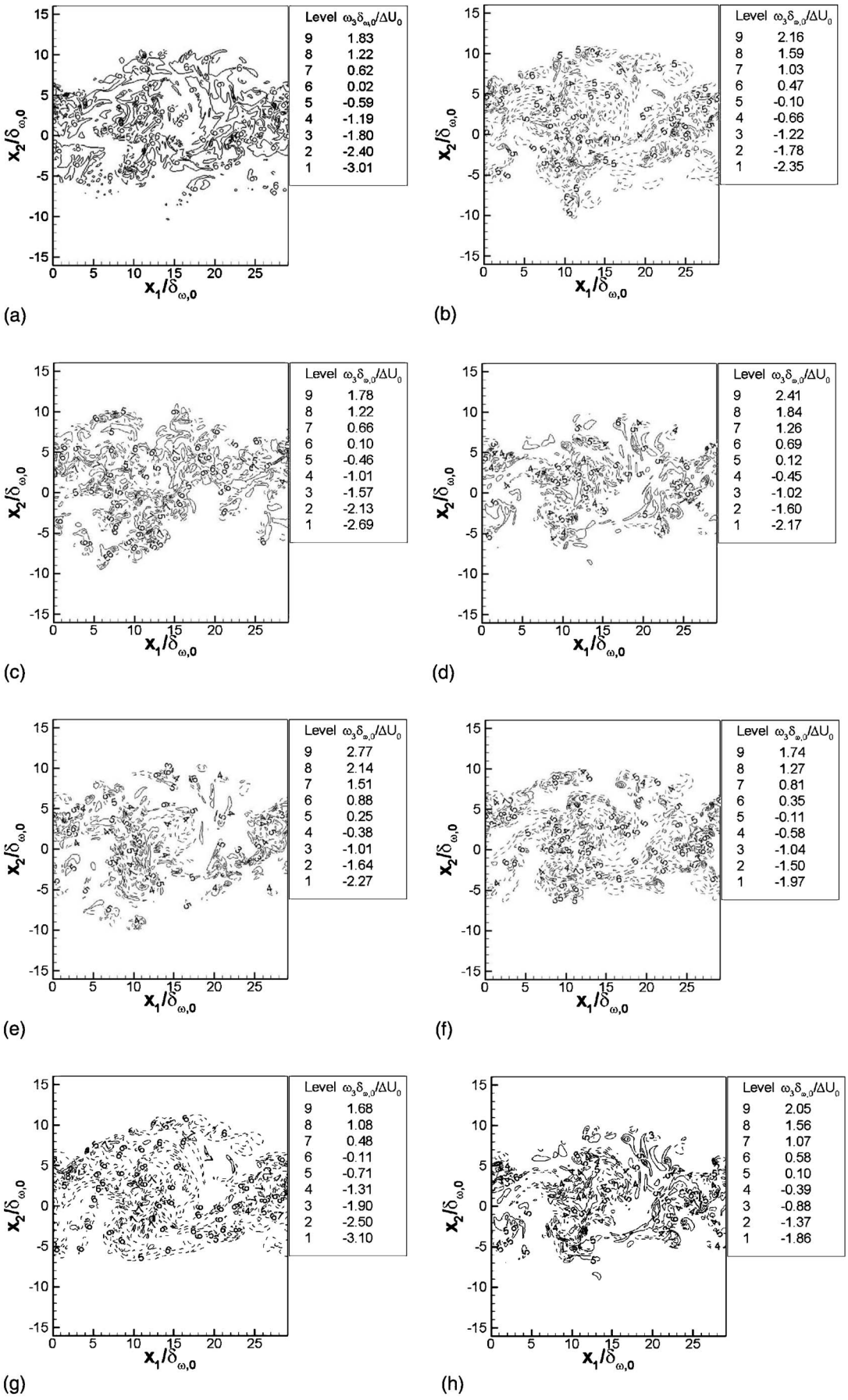

FIG. 11. Spanwise vorticity in the $x_3/L_3=0.5$ plane at t_{tr}^*: (a) die375ML2R5, (b) die400ML2R5, (c) die375ML5R5, (d) rp1400ML2R5, (e) jetA375ML2R5, (f) jetA400ML2R5, (g) jp7375ML2R5, and (h) jp7400ML2R5. Dashed lines represent negative vorticity values.

it is not only the sign of each of the two contributions that is important, but also their spatial variation that influences the sign of the source term. Although a direct relationship between liquid volatility and the sign of the source term is not immediately apparent, we note that for a very volatile liquid such as Jet A, $[\nabla\times(\mathbf{S}_{\mathrm{mom}}/\rho)]_3$ evidently becomes smaller with increasing T_0, whereas for a relatively much less volatile liquid, such as diesel, the vorticity source term becomes larger with increasing T_0. Because JP-7 and RP-1 follow the diesel trend, what seems to be the determining factor in this variation is the lightest species entering the composition of the liquid (see Fig. 2) rather than the width of the composition PDF. This T_0 effect on the vortical activity should be contrasted to the insensitivity observed in the pretransitional simulations of Le Clercq and Bellan,[15] indicating that this aspect is intimately related to the turbulence production through the drop/flow interaction.

b. Thermodynamics. The Y_v contours are shown in Fig. 12 for the same simulations illustrated in Fig. 8. The heterogeneity of the vapor distribution is noteworthy in all cases, with the larger values generally confined to the lower stream. As either T_0 or ML_0 increases [Figs. 12(a)–12(c)], the maximum Y_v increases, but this effect is a much stronger function of T_0 than of ML_0 because an augmentation in T_0 promotes single-drop evaporation through enhanced heat transfer, whereas the opposite happens at a more elevated ML_0 due to limitations on heat transfer from a gas phase with a fixed amount of heat. The larger maximum Y_v at $\mathrm{ML}_0=0.5$ compared to $\mathrm{ML}_0=0.2$ is thus a consequence of N_0, which affects $N\dot{m}$. Examination of the Y_v field structure shows increased heterogeneity with increasing T_0 or ML_0, with regions of the largest Y_v penetrating well into the mixing layer and reaching its boundary adjacent to the upper stream while pockets of negligible Y_v embed deep into the mixing layer. Concomitantly, regions of low Y_v are now present as isolated pockets in the lower stream. At fixed T_0 and ML_0, the maximum Y_v increases with increasing fuel volatility, while the structural complexity of the Y_v field decreases, which is attributed to the earlier evaporation that allows substantial small-scale mixing before the achievement of transition.

To entirely characterize the vapor, composition contours are displayed for θ_v in Fig. 13 and for σ_v in Fig. 14 corresponding to the simulations presented in Fig. 12. Compared to the pretransitional results of Le Clercq and Bellan,[15] the θ_v contours are considerably more contorted, with multiple locations, rather than a single location, of very high values throughout the mixing layer. With increasing T_0, the maximum value of θ_v increases [Figs. 13(a) and 13(b); Figs. 13(g) and 13(h)] due to the evaporation of the heavier components; the opposite occurs when ML_0 increases [Figs. 13(a) and 13(c)] due to the limitation in heat transfer, which prevents the release of heavier components. Generally, the range of θ_v values mirrors that in the initial liquid composition (Fig. 2) in that a narrow initial PDF range translates into a narrow range of θ_v values. For a narrower initial PDF having a larger-m component as its most volatile species [e.g., JP-7, for which $\gamma=93$ kg/kmol, shown in Fig. 13(g) relative to diesel, for which $\gamma=86$ kg/kmol, shown in Fig. 13(a)], the lower stream is uniquely composed of very light species due to the larger time lag necessary for the drops to reach a T_d value at which evaporation may proceed; at the more elevated ML_0, θ_v is also smaller in the lower stream, this being attributed to the lower T_d, which hinders evaporation of relatively less volatile species. The very close association between initial liquid composition and the magnitude and distribution of θ_v is best highlighted when examining Figs. 13(d) and 13(h) representing RP-1 and JP-7 at the same conditions: their almost coincidental PDFs of Fig. 2 results in virtually the same contour distribution and magnitude. Whether at $T_0=375$ K [Figs. 13(a), 13(e), and 13(g)] or at $T_0=400$ K [Figs. 13(b), 13(d), 13(f), and 13(h)], the heterogeneity of the θ_v distribution increases with decreasing PDF width.

Parallel contour plots of σ_v add more details to the information on the vapor composition. For all simulations, σ_v displays a complex distribution with generally small values in either stream, and intermediate and high values confined to the mixing layer. Notable exceptions are the baseline diesel simulation [Fig. 14(a)] and that with $\mathrm{ML}_0=0.5$ [Fig. 14(c)], where the upper stream exhibits larger σ_v than the lower stream, this being a manifestation of the lower stream condensation rather than implying that the upper stream σ_v is heterogeneous. Whereas in the pretransitional study of Le Clercq and Bellan[15] the locations of maximum θ_v and σ_v entirely coincided, here this is no longer the case. Although the intersection of the maximum-value θ_v and σ_v locations is not null in corresponding plots of Figs. 13 and 14, there is a considerable number of locations of maximum θ_v value that do not correspond to a location of maximum σ_v value, and vice versa. After substantial evaporation, when only the heavier species remain in a drop, the evolved turbulence is responsible for transporting that drop in regions where the vapor composition may be relatively uniform, and thus the local drop evaporation will result at that location in a large θ_v but relatively small σ_v [e.g., Figs. 13(a), 13(e), and 13(g) compared to Figs. 14(a), 14(e), and 14(g), respectively]. Conversely, drops at intermediary stages of evaporation may be brought by turbulence in a region of strong composition nonuniformity, thereby creating through evaporation a location of intermediary θ_v values and high σ_v values [i.e., Fig. 13(f) compared to Fig. 14(f)]. Scrutiny of Figs. 14(d) and 14(f) makes it clear that, unlike for θ_v, here there is no longer as strong a relationship between the initial liquid-composition PDF and the σ_v magnitude, although the qualitative aspect and the relative structure of the σ_v distribution are still closely related to this PDF. Increasing T_0 [Figs. 14(a) and 14(b), Figs. 14(e) and 14(f), and Figs. 14(g) and 14(h)] results in the maximum σ_v increasing, and this effect is stronger with decreased fuel volatility (diesel versus all kerosenes) because this promotes the release of an increasing range of heavier components from drops, as seen when comparing Figs. 13(a) and 13(b).

The general picture that emerges is that of the importance of both drop/turbulent-flow interaction and initial liquid-composition PDF in determining the vapor distribution and local composition. Both T_0 and ML_0 couple nonlinearly with that interaction and with the initial liquid-composition PDF.

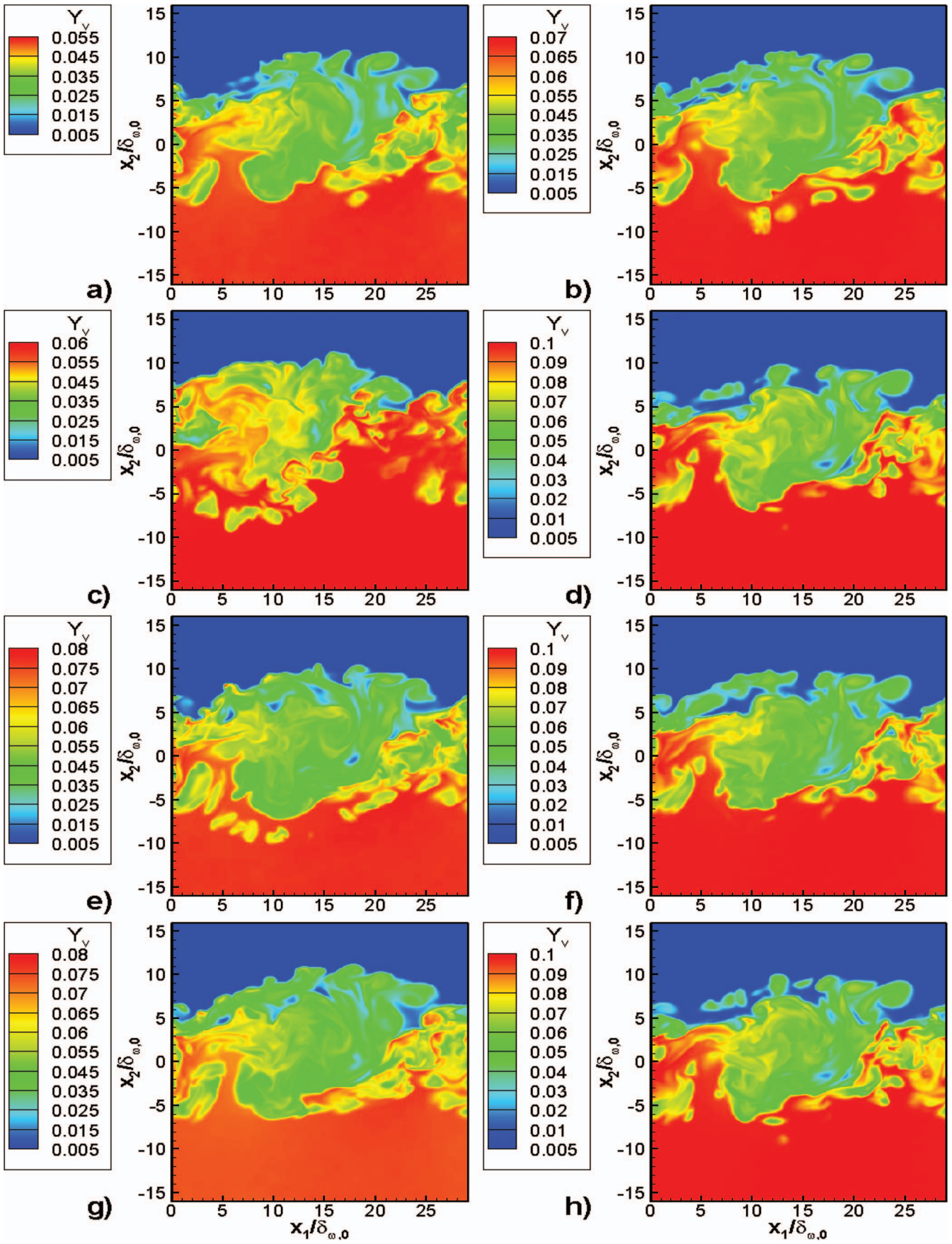

FIG. 12. (Color) Vapor mass fraction in the between-the-braid plane ($x_3/L_3=0.5$) at t_{ti}^*: (a) die375ML2R5, (b) die400ML2R5, (c) die375ML5R5, (d) rp1400ML2R5, (e) jetA375ML2R5, (f) jetA400ML2R5, (g) jp7375ML2R5, and (h) jp7400ML2R5.

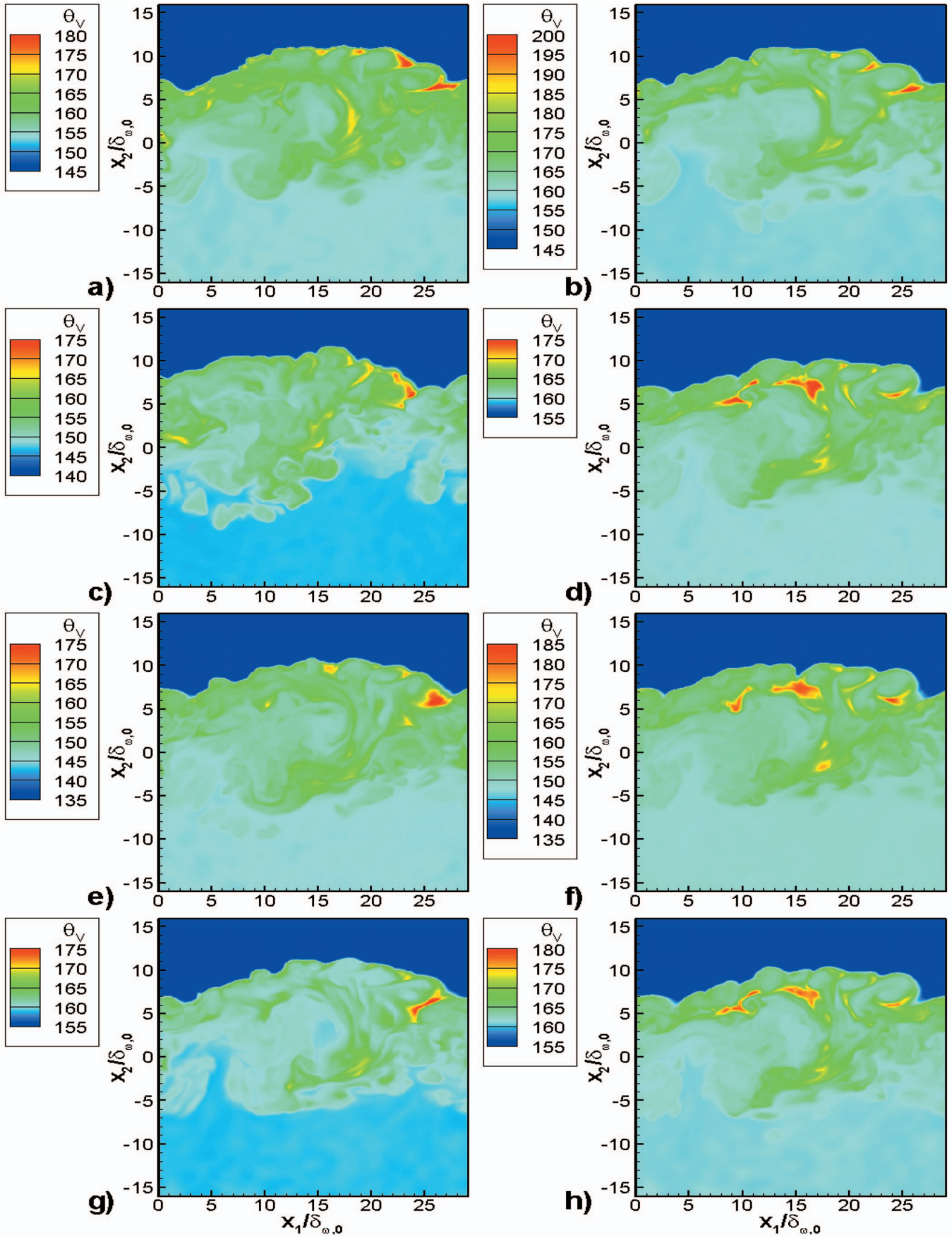

FIG. 13. (Color) Vapor mean molar mass (kg/kmol) in the between-the-braid plane ($x_3/L_3=0.5$) at t_{tr}^*: (a) die375ML2R5, (b) die400ML2R5, (c) die375ML5R5, (d) rp1400ML2R5, (e) jetA375ML2R5, (f) jetA400ML2R5, (g) jp7375ML2R5, and (h) jp7400ML2R5.

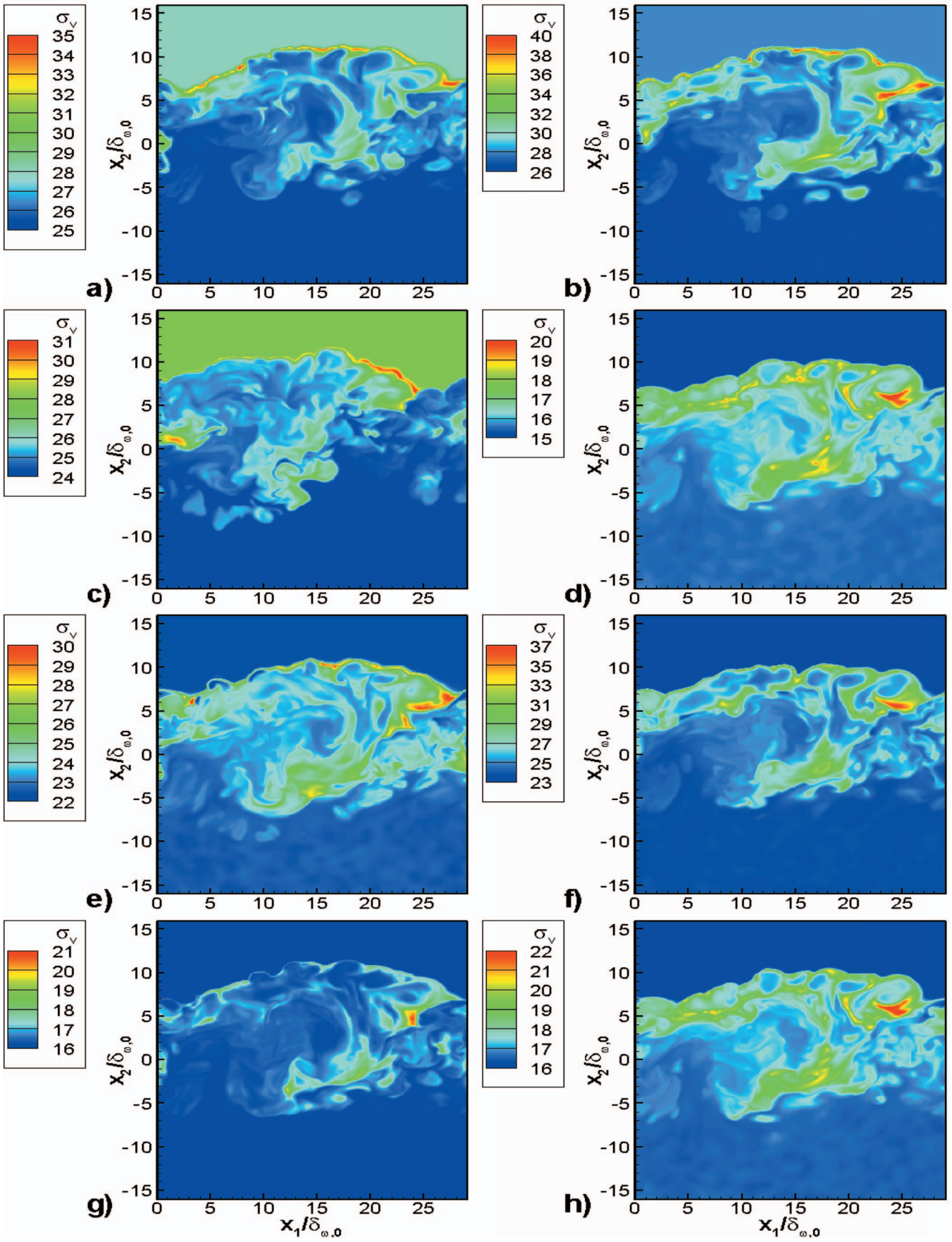

FIG. 14. (Color) Standard deviation of the vapor composition (kg/kmol) in the $x_3/L_3=0.5$ plane at t_{tr}^*: (a) die375ML2R5, (b) die400ML2R5, (c) die375ML5R5, (d) rp1400ML2R5, (e) jetA375ML2R5, (f) jetA400ML2R5, (g) jp7375ML2R5, and (h) jp7400ML2R5.

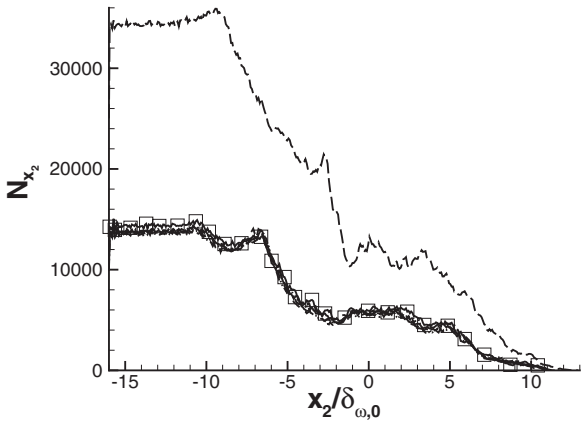

FIG. 15. Homogeneous (x_1,x_3) plane average number of drops at t^*_{tr}. The curve labels are listed in the Fig. 3 caption.

C. Liquid and vapor first-order statistics

1. Statistics related to the drops

a. Thermodynamics. Figure 15 displays the homogeneous (x_1,x_3) plane average number of drops, N_{x_2}, at t^*_{tr}. For a specified x_2, the value of N_{x_2} represents the number of drops in the region $(x_2-\Delta x_2/2, x_2+\Delta x_2/2)$. Clearly, for $ML_0=0.2$, in the lower stream (qualitatively here meaning $x_2/\delta_{\omega,0}<-10$) and in the mixing layer (qualitatively here meaning $-10\leqslant x_2/\delta_{\omega,0}<7$) there is a very large number of drops, and thus all drop statistics performed at these locations are meaningful. With increasing $x_2/\delta_{\omega,0}$ beyond $x_2/\delta_{\omega,0}=7$, the quality of the statistics will deteriorate. For $ML_0=0.5$, the number of drops in the lower stream increases proportionally to the ML_0 augmentation and in the mixing layer, despite the local (i.e., with $x_2/\delta_{\omega,0}$) fluctuations, the number of drops remains proportional to the ML ratio.

Statistics over a specified drop ensemble may be of interest either for drop-defined quantities, in which case the concept is straightforward, or for gas-defined quantities interpolated at the drop locations, in which case it represents the drop's far-field value. From a gas-defined quantity, A, interpolated through $\mathcal{I}$ to drop locations, resulting in the quantity $A^{\mathcal{I}}$, three types of drop ensemble averages can be defined as shown in Table III. For example, ρ_n can be interpolated to the drop locations to obtain $\rho_n^{\mathcal{I}}$, and one can further calculate the number of drops per computational cell (i.e., inside ΔV_q), $n_c \equiv [\rho_n^{\mathcal{I}}]_c = \rho_n^{\mathcal{I}} \times \Delta V_q$, where $\Delta V_q = \Delta x_1 \times \Delta x_2 \times \Delta x_3$ is the cell volume defined in Sec. II C. Drop ensemble averages of n_c, T_d, θ_l, and σ_l and their standard deviations are presented in Fig. 16.

TABLE III. Definition of several types of drop-related averaging for a quantity A defined at grid nodes.

$A^{\mathcal{I}} \Rightarrow A^{\mathcal{I}}$	↗	$\{\{A^{\mathcal{I}}\}\}$	quantity averaged over all N drops in the volume
	→	$\{A^{\mathcal{I}}\}$	quantity averaged over N_{x_2} drops in homogeneous (x_1,x_3) planes
	↘	$[A^{\mathcal{I}}]_c$	quantity averaged over drops in the discretization volume $\Delta x_1 \times \Delta x_3 \times \Delta x_3$

Despite the large number of drops in the lower stream, $\{n_c\}<1$ ({} defined in Table III) for all simulations (for readability, only a restricted selection of simulations is shown in Fig. 16(a)). In the mixing layer, $\{n_c\}<1.5$ for $ML_0=0.2$ and $\{n_c\}\lesssim 2$ for $ML_0=0.5$, showing again the consistency of our assumptions regarding the volumetric loading past the initial condition, particularly since $\{\{V_d\}\}/\{\{V_{d,0}\}\}$ has considerably decreased from unity [as conservatively indicated by $\{\{D^2\}\}_{ml}/\{\{D_0^2\}\}$ in Fig. 6(b), the mixing layer region being that where both $\{n_c\}$ and the standard deviation, $(\{n_c^2\}-\{n_c\}^2)^{0.5}$ shown in Fig. 16(b), are largest]; the same result prevails for $x_2/\delta_{\omega,0}>7$, although the statistics are not considered converged.

For all simulations at $ML_0=0.2$ and $T_0=375$ K, $\{T_d\}/T_{d,0}$ decreases in the lower stream from its initial value [Fig. 16(c)] and this reduction is by happenstance similar for diesel, RP-1, and JP-7, while for Jet A, the most volatile liquid, slightly smaller values are obtained. This reduction is due to the immediate evaporation of the most volatile species, and since Jet A contains more volatile species than each of the other liquids (Fig. 2), the decrease in $\{T_d\}/T_{d,0}$ is largest. Expectably, with increasing T_0, $\{T_d\}/T_{d,0}$ is larger and even exceeds unity at $T_0=400$ K, indicating that heat transfer to the drops combined with condensation more than compensates for that lost from evaporation [$\{\sigma_l\}/\sigma_{l,0}<1$ in Fig. 16(g)]. Conversely, when $ML_0=0.5$, $\{T_d\}/T_{d,0}$ is further depressed due to the same amount of heat now being available for an increased number of drops. ML_0 trends similar to those in the lower stream are observed throughout the mixing layer; with the important difference being that however in this region of high drop/flow interaction, with increasing $x_2/\delta_{\omega,0}$ there is increasing coincidence among all kerosenes, which is attributed to the similar species in the three kerosenes once the very volatile ones have been released, that is, to the coincidence of the high-m region for Jet A, RP-1, and JP-7 (Fig. 2). With increasing $x_2/\delta_{\omega,0}$ beyond the lower stream, and for $T_0=400$ K, $\{T_d\}/T_{d,0}$ augments at a higher rate than at $T_0=375$ K, this being explained by the hotter air entrained into the mixing layer from the upper stream, which promotes drop heating. Whereas $(\{T_d^2\}-\{T_d\}^2)^{0.5}/T_{d,0}$ is minimal in the lower stream [Fig. 16(d)], in the mixing layer it abruptly increases by approximately a factor of 10, indicating the great $\{T_d\}/T_{d,0}$ variability in this region of high drop/turbulence interaction; the plateau-like value exhibited by the standard deviation across the entire mixing layer is indicative of nearly uniform variability. The least $\{T_d\}/T_{d,0}$ variability occurs for RP-1 and JP-7, portraying their narrow composition, followed by diesel and Jet A, which have wider PDFs. The $\{T_d\}/T_{d,0}$ variability declines with increasing ML_0 and augments with higher T_0, being a direct consequence of the reduced/increased availability of heat for each drop in the layer.

The drop composition statistics are illustrated in Figs. 16(e) and 16(f) for $\theta_l/\theta_{l,0}$ and in Figs. 16(g) and 16(h) for $\sigma_l/\sigma_{l,0}$. The lower stream is characterized by a uniform $\{\theta_l\}/\theta_{l,0}>1$, resulting from the early evaporation of the most volatile species, with the largest values reached by diesel and Jet A that contain more volatile species than RP-1 and JP-7.

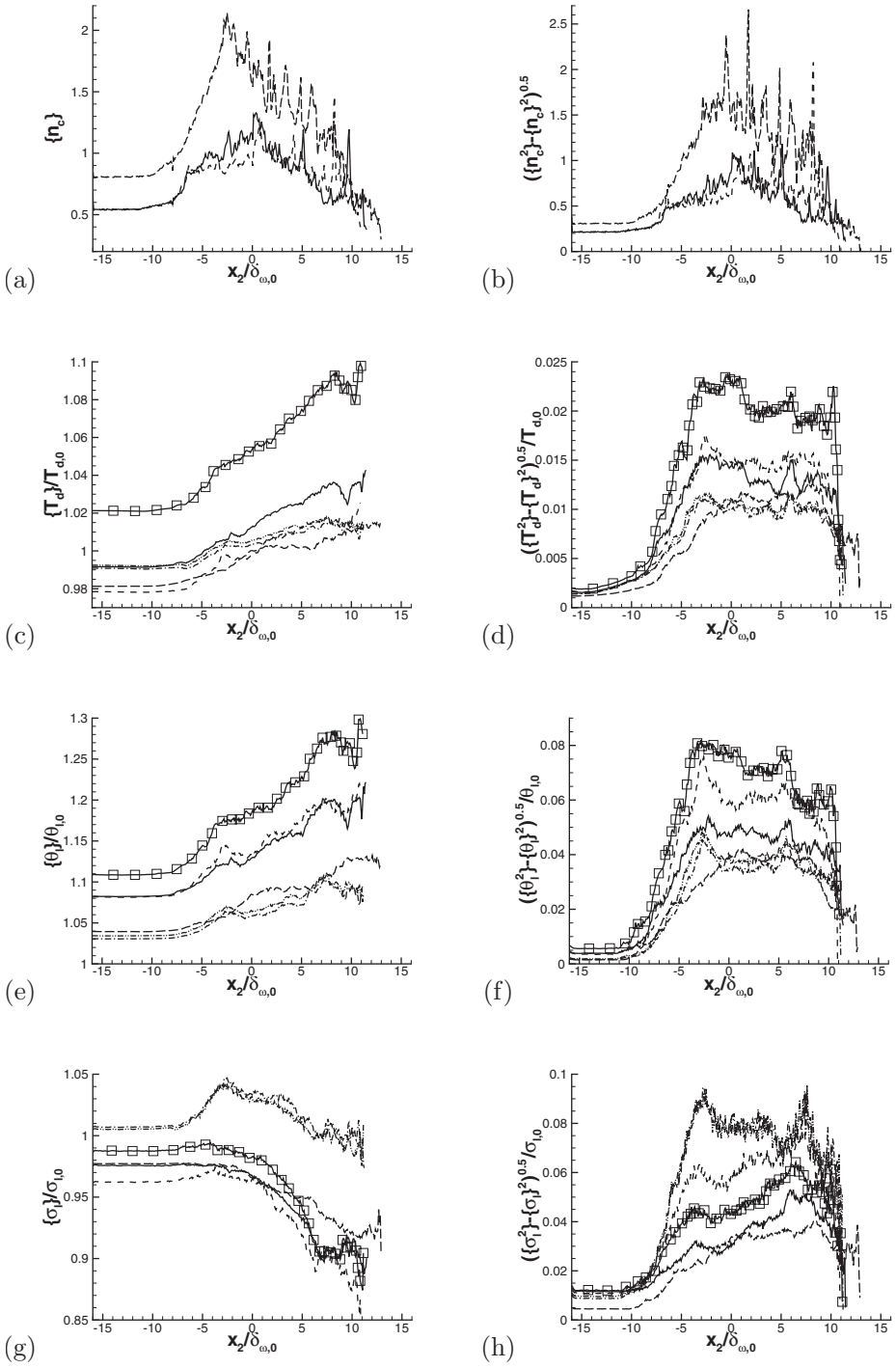

FIG. 16. Homogeneous (x_1, x_3) plane-average drop statistics at t_{tr}^*. For die375ML2R5, die375ML5R5, and jetA375ML2R5: (a) and (b). (a) $\{n_c\}$, (b) $[\{n_c^2\}-(\{n_c\})^2]^{0.5}$. For die375ML2R5, die375ML5R5, die400ML2R5, jetA375ML2R5, rp1375ML2R5, and jp7375ML2R5: (c)–(h). (c) $\{T_d\}/T_{d,0}$, (d) $[\{T_d^2\}/T_{d,0}^2-(\{T_d\}/T_{d,0})^2]^{0.5}$, (e) $\{\theta_l\}/\theta_{l,0}$, (f) $[\{\theta_l^2\}/\theta_{l,0}^2-(\{\theta_l\}/\theta_{l,0})^2]^{0.5}$, (g) $\{\sigma_l\}/\sigma_{l,0}$, (h) $[\{\sigma_l^2\}/\sigma_{l,0}^2-(\{\sigma_l\}/\sigma_{l,0})^2]^{0.5}$. Curve labels listed in the Fig. 3 caption.

However, while $\{\sigma_l\}/\sigma_{l,0}<1$ for diesel and Jet A, indicative of evaporation, $\{\sigma_l\}/\sigma_{l,0}>1$ for RP-1 and JP-7 indicative of condensation, both with respect to the initial condition. Increasing ML_0 or T_0 has opposite effects on $\{\theta_l\}/\theta_{l,0}$ in that it decreases/increases its value, portraying reduced/enhanced evaporation with respect to the baseline case, whereas it has a qualitatively similar, increasing effect on $\{\sigma_l\}/\sigma_{l,0}$ with the influence of ML_0 being much weaker. It is clear that within the restricted parametric range investigated, ML_0 has in the lower stream a much stronger influence on $\{\theta_l\}/\theta_{l,0}$ than on $\{\sigma_l\}/\sigma_{l,0}$, while the opposite is true for T_0. Both $(\{\theta_l^2\}-\{\theta_l\}^2)^{0.5}/\theta_{l,0}$ and $(\{\sigma_l^2\}-\{\sigma_l\}^2)^{0.5}/\sigma_{l,0}$ are minimal within the lower stream, consistent with the low level of heterogeneity encountered in this region. At $ML_0=0.2$ and $T_0=375$ K, proceeding into the mixing layer, $\{\theta_l\}/\theta_{l,0}$ augments with $x_2/\delta_{\omega,0}$ at a larger rate for diesel and Jet A than for the other two kerosenes, which is evidence of increased evaporation of the most volatile species in diesel and Jet A that are not part of the RP-1 and JP-7 compositions. In contrast to the $\{\theta_l\}/\theta_{l,0}$ variation, for $\{\sigma_l\}/\sigma_{l,0}$ two distinct behaviors are apparent: RP-1 and JP-7, which have the narrower compositions, have experienced increasing condensation with increasing $x_2/\delta_{\omega,0}$

in the lower part of the mixing layer (i.e., $\{\sigma_l\}/\sigma_{l,0}>1$ and increases), followed by reduced condensation with increasing $x_2/\delta_{\omega,0}$ (i.e., $\{\sigma_l\}/\sigma_{l,0}>1$ and decreases), and finally by evaporation in the upper part of the mixing layer (i.e., $\{\sigma_l\}/\sigma_{l,0}<1$ and decreases). In contrast, for diesel and Jet A, overall evaporation has occurred (i.e., $\{\sigma_l\}/\sigma_{l,0}<1$), which was enhanced with increasing $x_2/\delta_{\omega,0}$ (i.e., $\{\sigma_l\}/\sigma_{l,0}$ decreases). The nonmonotonic behavior for the narrower PDF kerosenes is conjectured to result from a combination of the smaller T_d value in the lower part of the mixing layer and of entrainment into this region of the very volatile species that have evaporated early into the lower stream and are here encountering favorable conditions for condensation. While both evaporation and condensation may concomitantly occur for diesel and Jet A, the larger separation in saturation pressure between the early evaporated species residing in the lower stream and the intermediate species released in the mixing layer leads to a larger loss of species through evaporation. Neither a change of value in ML_0 nor in T_0 results in qualitative changes in the variation of $\{\theta_l\}/\theta_{l,0}$ and $\{\sigma_l\}/\sigma_{l,0}$ with $x_2/\delta_{\omega,0}$, and even the quantitative rate of augmentation trends remains for $\{\theta_l\}/\theta_{l,0}$. However, $\{\sigma_l\}/\sigma_{l,0}$ exhibits a stronger decay at the higher T_0, indicative of stronger evaporation, whereas the opposite occurs at the larger ML_0. The larger $(\{\theta_l^2\}-\{\theta_l\}^2)^{0.5}/\theta_{l,0}$ and $(\{\sigma_l^2\}-\{\sigma_l\}^2)^{0.5}/\sigma_{l,0}$ values, by approximately a factor of 10, in the mixing layer compared to the lower stream are reminiscent of the enhanced heterogeneity of the layer. Of note, among all liquids the largest values of $(\{\theta_l^2\}-\{\theta_l\}^2)^{0.5}/\theta_{l,0}$ occur for diesel, closely followed by RP-1 and JP-7, with Jet A showing distinctively less $\{\theta_l\}/\theta_{l,0}$ variability in the lower part of the mixing layer, apparently due to its increased volatility with respect to all other liquids. Within the range explored, either changes in ML_0 or T_0 lead to substantially (~60%) more elevated values of $(\{\theta_l^2\}-\{\theta_l\}^2)^{0.5}/\theta_{l,0}$, indicating that the diversity of $\{\theta_l\}/\theta_{l,0}$ values will be considerably greater in real combustors where T_0 is much larger. Contrasting to the variation of $(\{\theta_l^2\}-\{\theta_l\}^2)^{0.5}/\theta_{l,0}$ with fuel composition, $(\{\sigma_l^2\}-\{\sigma_l\}^2)^{0.5}/\sigma_{l,0}$ is largest for RP-1 and JP-7 because their narrow composition means that either evaporation or condensation of a very small number of species can greatly affect the liquid PDF. This interpretation is supported by the fact that continuing in decreasing order of magnitude are the $(\{\sigma_l^2\}-\{\sigma_l\}^2)^{0.5}/\sigma_{l,0}$ values for Jet A and diesel, an ordering aligned with the width of their composition, and that the diesel results fall considerably lower than those of the three kerosenes, consistent with its much larger PDF width.

b. Size and organization. The information provided by the contour plots of Fig. 8 was of a pictorial nature and did not provide quantitative information about drop size and organization according to position within the volume. Such quantitative information is first provided in Fig. 17 through St, which was defined in Sec. III and is here rewritten as

$$\mathrm{St}=\frac{\rho_l}{18\rho_{g,0}}\mathrm{Re}_0\frac{D^2}{\delta_{\omega,0}^2} \tag{23}$$

using the definition of Re_0 to eliminate μ. From Eq. (23), it is clear that because all other quantities are initially specified, the variation of St is determined by that of D^2. Illustrated in Figs. 17(a) and 17(b) are $\{\mathrm{St}\}$ and $(\{\mathrm{St}^2\}-\{\mathrm{St}\}^2)^{0.5}$, respectively, at t_{tr}^*. Regarding the drop preferential organization, Le Clercq and Bellan[10] have discussed how the second invariant of the deformation tensor for compressible flow,

$$II_u=-\tfrac{1}{2}\left[(S_{ij}S_{ij}-S_{kk}S_{ll})-\tfrac{1}{2}\omega_i\omega_i\right], \tag{24}$$

where the strain rate is

$$S_{ij}=\frac{1}{2}\left(\frac{\partial u_i}{\partial x_j}+\frac{\partial u_j}{\partial x_i}\right), \tag{25}$$

is conducive to distinguishing portions of the flow that are of rotational or compressible nature, corresponding to $II_u>0$, from regions where strain dominates, corresponding to $II_u<0$. Thus $II_u^{\mathcal{I}}$ is a measure of II_u at the drop locations, and the sign of this quantity indicates whether the drop is in a region of rotation and compression, or in a region of strain. Plots of $\{II_u^{\mathcal{I}}\}/(\Delta U_0/\delta_{\omega,0})^2$ and $(\{(II_u^{\mathcal{I}})^2\}-\{II_u^{\mathcal{I}}\}^2)^{0.5}/(\Delta U_0/\delta_{\omega,0})^2$ at t_{tr}^* are presented in Figs. 17(c) and 17(d).

The average drop size is evidently approximately constant throughout the lower stream and continuously decreases from the lower stream to the mixing layer and throughout the mixing layer in the direction of the upper stream. In light of the $\{n_c\}$ variation discussed in conjunction with Fig. 16(a), the larger number of drops per cell in the mixing layer is balanced by their smaller volume, which still leads to a negligible ratio of the drop-to-cell volume, and consequently negligible computational error in these Eulerian/Lagrangian simulations. The fact that at all locations $\{\mathrm{St}\}<3$, which is the initial volumetric mean, is indicative of the drop-size reduction due to evaporation. In the lower stream, $(\{\mathrm{St}^2\}-\{\mathrm{St}\}^2)^{0.5}$ is smaller than the initial volumetric value of 0.5, meaning that the drop size distribution is more uniform, whereas the opposite is evident in the mixing layer, which is a manifestation of the increased size polydispersity resulting from the drop/flow interaction. As expected, both $\{\mathrm{St}\}$ and $(\{\mathrm{St}^2\}-\{\mathrm{St}\}^2)^{0.5}$ decrease with liquid volatility or increasing T_0, and increase with larger ML_0.

Figures 17(c) and 17(e) show that except for the lower stream where $II_u=0$ (lack of strain and vorticity), in the entire mixing layer the drops reside in strain-dominated locations, consistent with the findings of Squires and Eaton.[37] This result gives perspective to the finding of Le Clercq and Bellan[10] that most drops in the volume accumulate in regions of $II_u\simeq 0$, showing that the result was biased by the much larger number of drops in the lower stream (Fig. 15). The present results show that with increasing volatility or T_0 and with decreasing ML_0, the drops generally reside in regions of increasing strain. As either T_0 or ML_0 increase, or as the volatility increases (RP-1 and JP-7 not displayed), sharp peaks of larger-strain regions populated with drops are evident, remnant of the parallel sharp peaks observed in Fig. 16(a). Based on these findings, the conjecture is that the much larger T_0 in combustors is conducive to generating very-high-strain drop-laden regions. Considering the $x_2/\delta_{\omega,0}$ variation of $(\{(II_u^{\mathcal{I}})^2\}-\{II_u^{\mathcal{I}}\}^2)^{0.5}/(\Delta U_0/\delta_{\omega,0})^2$ [Figs. 17(d) and 17(f)], it appears that the diversity of $\{II_u^{\mathcal{I}}\}/(\Delta U_0/\delta_{\omega,0})^2$ also

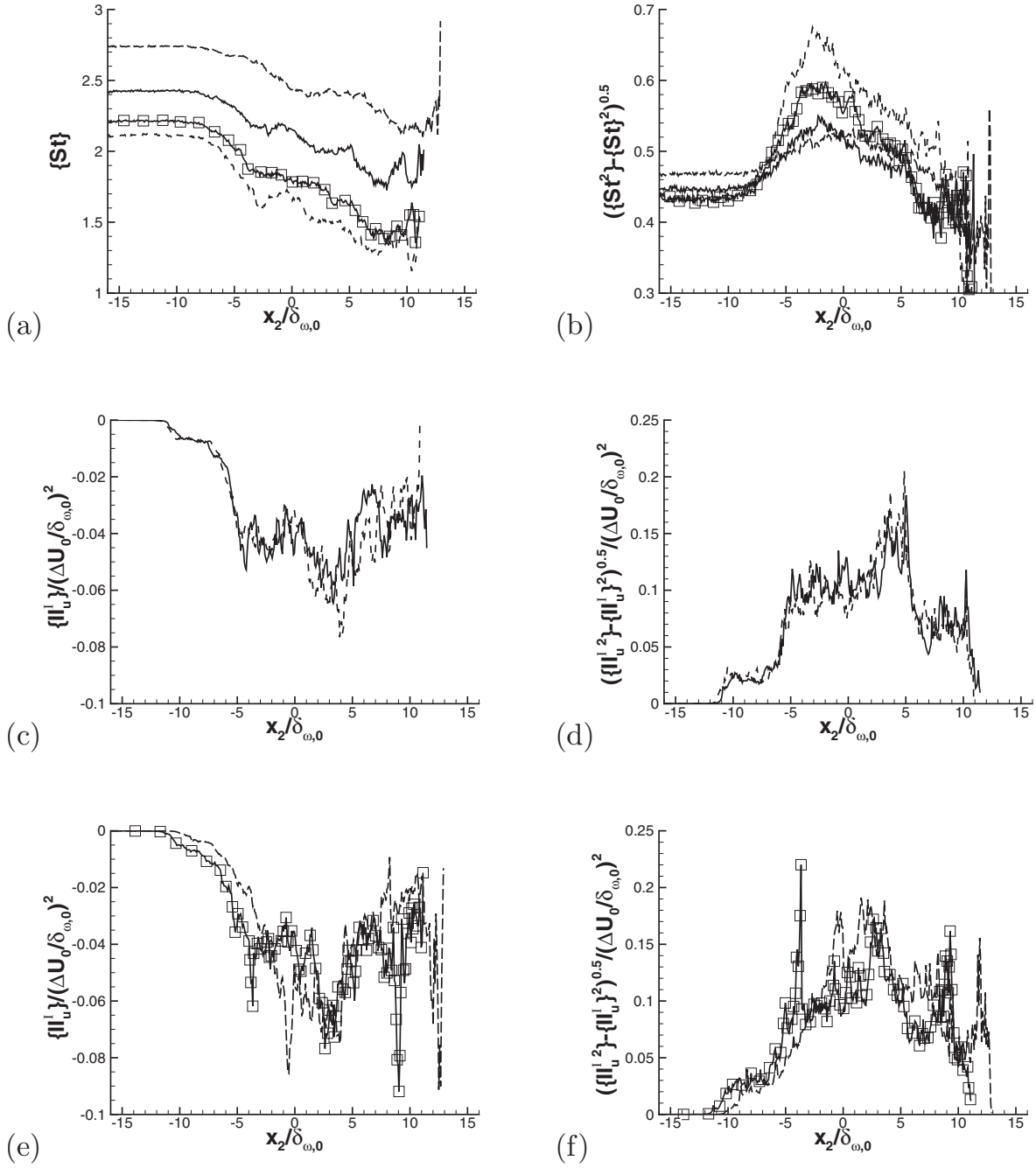

FIG. 17. Homogeneous (x_1,x_3) plane average drop statistics at t_{tr}^*. [(a) and (b)] die375ML2R5, die375ML5R5, die400ML2R5, and jetA375ML2R5; [(c) and (d)] die375ML2R5 and die375ML5R5; [(e) and (f)] die400ML2R5 and jetA375ML2R5. (a) St, (b) $[\{St^2\}-(\{St\})^2]^{0.5}$, (c) $\{II_u^T\}/(\Delta U_0/\delta_{\omega,0})^2$, (d) $[\{(II_u^T)^2\}-(\{II_u^T\})^2]^{0.5}/(\Delta U_0/\delta_{\omega,0})^2$. The curve labels are listed in the Fig. 3 caption.

increases with more elevated values of volatility, T_0 or ML_0, reinforcing the conclusion about combustors where large differences in properties will occur among locations where drops reside.

c. Probabilities. All homogeneous (x_1,x_3) plane averages show that the drop characteristics are strongly affected by the surrounding flow. To elucidate the influence of the location on the drops, PDFs are separately calculated over the lower stream and over the mixing-layer drop ensembles, and are displayed in Fig. 18. For figure readability, results are only shown for diesel and different T_0, as T_0 is considered important in projecting how the results might change at the very much higher T_0 in combustors. (For readability, the curve labels are specific to this figure and changed from those listed in the Fig. 3 caption.) Because variations with increased T_0 mimic those for liquids with increased volatility, the following results at $T_0=400$ K can also be interpreted as being applicable to the kerosenes.

The probability of a given number of drops per cell, whether in the lower stream or the mixing layer, is insensitive to T_0 as shown by $P(n_c)$ in Fig. 18(a). Independent of the two locations, the PDF peaks at about $n_c=0.6$, but is considerably wider for the mixing layer relative to the lower stream, consistent with Fig. 16(b). This is the consequence of

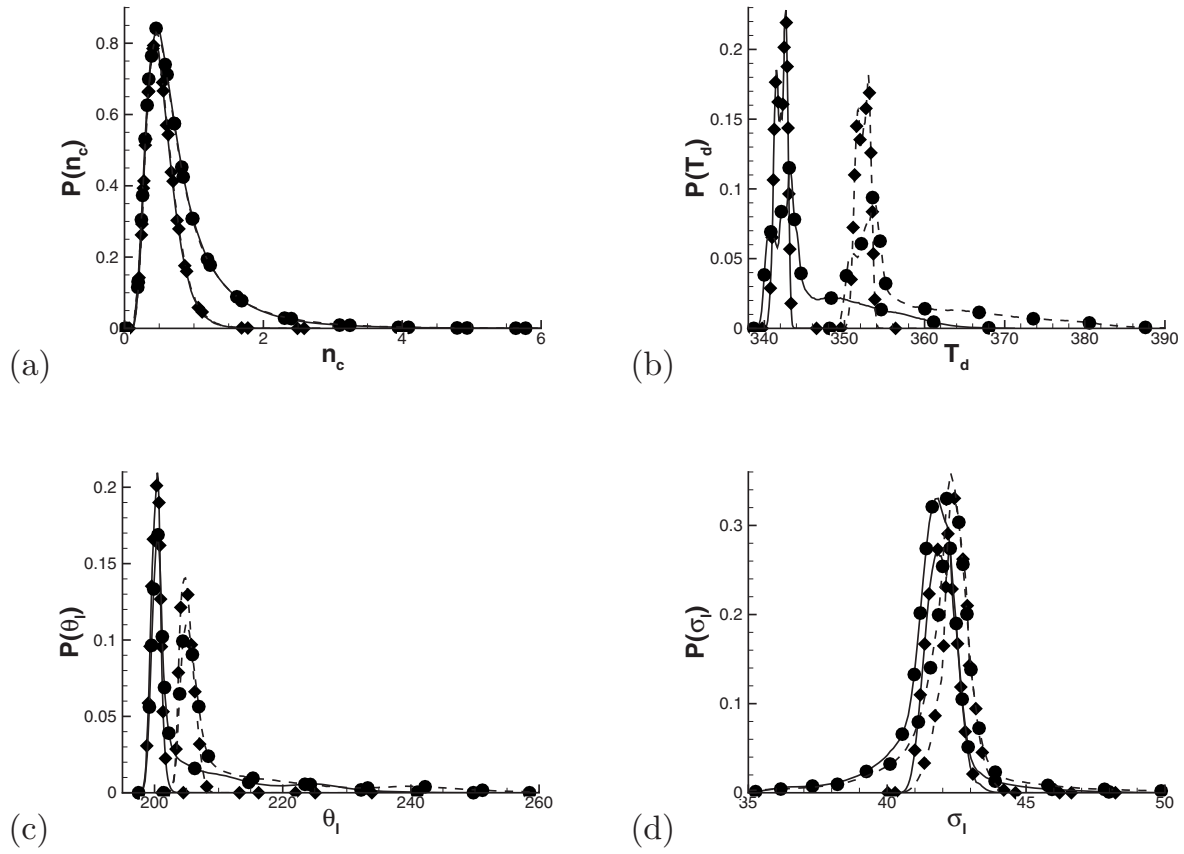

FIG. 18. Probabilities computed over the drop ensemble in the lower stream (♦) and in the mixing layer (●) for die375ML2R5 and die400ML2R5 at t_{tr}^{*}. The criterion for defining the lower stream and the mixing layer is that of Sec. IV A 2. The curve labels are changed from those listed in the Fig. 3 caption: die375ML2R5 ——— and die400ML2R5 – – –. (a) $P(n_c)$, (b) $P(T_d)$, (c) $P(\theta_l)$ and (d) $P(\sigma_l)$.

drop segregation in the mixing layer, as seen in Figs. 17(c) and 17(e). In contrast, $P(T_d)$ in Fig. 18(b) exhibits high specificity both to T_0 and to the drop location. Independent of T_0, T_d has a much larger range of higher values in the mixing layer than in the lower stream. Also independent of T_0, in both regions, the PDF displays a major peak and then a minor peak at smaller T_d values; although the larger peak is at the same T_d value in both regions, in the mixing layer the minor peak is at inferior values than in the lower stream, making the lower-stream PDF wider in the region of most probability. The dual T_d peak corresponds to regions of relatively low T in the central streamwise portion of the domain caused by the lower p at the center of the final vortex (not shown), surrounded by regions of higher p and thus larger T. Figure 9(a) clearly depicts the dual T_d preferential values in the lower portion of the mixing layer. The major peak indicates a preferential value, which for T_0=375 K is in the lower stream slightly inferior to T_0. The location of this minor peak, which indicates the lower boundary of the range of most probable values, shows that even within these most probable values, the mixing layer has more variability than the lower stream, consistent with the physical understanding derived from scrutiny of Fig. 16(d).

The composition information presented in Figs. 18(c) and 18(d) shows that independent of T_0, $P(\theta_l)$ peaks at the same θ_l but is much narrower in the lower stream than in the mixing layer, consistent with the similar history of all drops in the lower stream and the diversity of drop history for the mixing layer drops, as clearly seen in Fig. 9(b). At larger T_0, $P(\theta_l)$ is translated to the range of larger θ_l as the more volatile species have been released earlier from the drops, and its width increases, consistent with the information of Fig. 16(f). Of note, some drops have a liquid mean molar mass as heavy as 260 kg/kmol, and this value increases to ~300 kg/kmol at T_0=400 K (not shown). Thus, for the much larger T_0 in combustors, it is expected that the mean molar mass of the liquid will increase from the present values, leading to coke or cenosphere formation when species as heavy as ~500 kg/kmol have a non-negligible presence in the drop.[38–40] Complementary to $P(\theta_l)$, $P(\sigma_l)$ shows that the preferred value is similar for both lower-stream and mixing-layer regions, and that the location of the peak slightly increases with larger T_0. Independent of T_0, the $P(\sigma_l)$ width is larger in the mixing layer, consistent with the information in Fig. 16(h).

2. Vapor statistics

Homogeneous-plane averages of $\theta_v/\theta_{v,0}$ and $\sigma_v/\sigma_{v,0}$ at t_{tr}^{*} are displayed in Fig. 19. For both $\langle\theta_v\rangle/\theta_{v,0}$ and $\langle\sigma_v\rangle/\sigma_{v,0}$, the lower stream is characterized by a uniform distribution, with the values increasing into and culminating in the mixing layer, then decreasing and reaching unity in the upper stream.

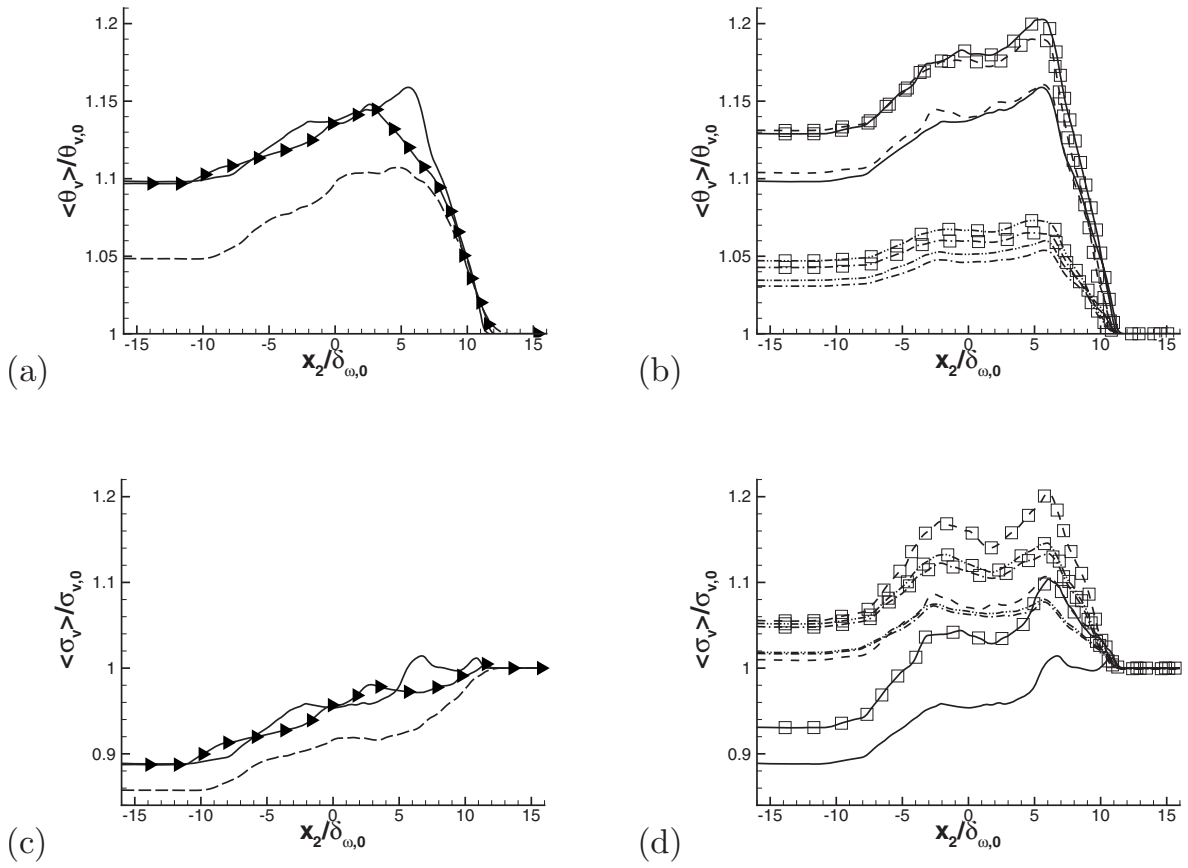

FIG. 19. Homogeneous (x_1, x_3) plane average vapor composition at t^*_{tr} for all transitional simulations and $t^*=100$ for die375ML2R2: [(a) and (b)] $\langle\theta_v\rangle/\theta_{v,0}$ and [(c) and (d)] $\langle\sigma_v\rangle/\sigma_{v,0}$. [(a) and (c)] die375ML2R2, die375ML2R5, and die375ML5R5; [(b) and (d)] die375ML2R5, die400ML2R5, jetA375ML2R5, jetA400ML2R5, rp1375ML2R5, rp1400ML2R5, jp7375ML2R5, and jp7400ML2R5. The curve labels are listed in the Figs. 3 and 5 captions.

As ML_0 increases [Figs. 19(a) and 19(c)], both $\langle\theta_v\rangle/\theta_{v,0}$ and $\langle\sigma_v\rangle/\sigma_{v,0}$ decrease throughout the lower stream and mixing layer, indicative of evaporation being relatively restricted to the more volatile, lighter species. The magnitudes of $\langle\theta_v\rangle/\theta_{v,0}$ and $\langle\sigma_v\rangle/\sigma_{v,0}$ are mildly sensitive to an augmentation in Re_0 [Figs. 19(a) and 19(c)], as evidenced by similar values at different Re_0 both in the lower stream and in the lower part of the mixing layer. However, additional structure is observed at the higher Re_0 and the upper edge of the layer contains now heavier species, meaning that the composition is more heterogeneous.

Figure 19(b) shows that the diesel and Jet A $\langle\theta_v\rangle/\theta_{v,0}$ profiles coincide, independent of T_0, and that RP-1 and JP-7 results are very close at both values of T_0. We conjecture here that the coincidence of diesel and Jet A means that it is not only the width of the liquid composition PDF that matters under transitional conditions, differentiating the diesel and Jet A from RP-1 and JP-7, but also the identity of the most volatile species. Jet A experiences evaporation in the lower stream, as shown by $\langle\sigma_v\rangle/\sigma_{v,0}>1$ in Fig. 19(d), which together with the larger mean molar mass there indicates enhanced release of less volatile species. Across the layer, evaporation occurs for all kerosenes. However, for diesel condensation occurs except at the larger T_0, where evaporation prevails only at locations higher than approximately $x_2/\delta_{\omega,0}>5$ in the layer. The physical picture that emerges from consideration of $\langle\sigma_v\rangle/\sigma_{v,0}$ together with the $\langle\theta_v\rangle/\theta_{v,0}$ profiles is that of an accumulation of high molar mass species in the core of the layer, with a relatively narrower distribution than at both lower and upper layer boundaries. The composition at the lower boundary of the mixing layer does not have in the mean as high a molar mass as the layer core, but it has a wider species distribution, with presumably a multitude of highly volatile species entrained from the lower stream. At the upper mixing layer boundary, the composition is also wider than in the layer core, with a larger mean molar mass than either the core or the lower layer region, this being due to the higher-m species that evaporate once the very volatile and moderately volatile species have been released from the drops. These species have traversed the mixing layer to reach its upper boundary. This physical picture is consistent with that derived from examination of Fig. 9(b).

D. Dissipation analysis

Because the energy spectra of Fig. 4 showed significant differences in the small-scale energy from the SC-liquid study of Okong'o and Bellan,[20] suggesting here a more pronounced small-scale dissipation, it is of interest to examine the irreversible entropy production, which is essentially the dissipation. Okong'o and Bellan[20] have shown that for a TP flow, additional to the semidefinite positive quadratic terms

in the SP dissipation, there are also source terms present; in the SC-liquid study of Ref. 20, the source terms entirely dominated the dissipation budget at transition. The mathematical form of the Ref. 20 dissipation still applies here, as the equations for ξ_{nv} are not involved in the derivation. Specifically, according to Ref. 20, the dissipation g is

$$g = g_{\mathrm{III}} + g_{\mathrm{II}} + g_{\mathrm{I,kine}} + g_{\mathrm{I,chpot}} + g_{\mathrm{visc}} + g_{\mathrm{temp}} + g_{\mathrm{mass}}, \tag{26}$$

$$g_{\mathrm{III}} = \frac{S_{en}}{T}, \quad g_{\mathrm{II}} = -\frac{u_i S_{\mathrm{mom},i}}{T}, \tag{27}$$

$$g_{\mathrm{I,kine}} = \frac{\frac{1}{2}u_i u_i S_{\mathrm{mass}}}{T}, \quad g_{\mathrm{I,chpot}} = -\frac{\mu_v S_{\mathrm{mass}}}{T},$$

$$g_{\mathrm{visc}} = \frac{2\mu}{T}\left(S_{ij} - \frac{1}{3}S_{kk}\delta_{ij}\right)\left(S_{ij} - \frac{1}{3}S_{ll}\delta_{ij}\right), \tag{28}$$

$$g_{\mathrm{temp}} = \frac{\lambda}{T^2}\frac{\partial T}{\partial x_j}\frac{\partial T}{\partial x_j},$$

$$g_{\mathrm{mass}} = \frac{R_a R_v}{Y_a Y_v (R_v Y_v + R_a Y_a)}\frac{1}{\rho \mathcal{D}}\left[-\frac{\partial (cX_v)}{\partial x_j}\right]\left[-\frac{\partial (cX_v)}{\partial x_j}\right], \tag{29}$$

where $R_v = R_u/\theta_v$ and $\mu_v = h_v - Ts_v$ is the chemical potential with s_v being the entropy of the pure vapor, which is calculated for a perfect gas as

$$s_v = \int C_{p,v}(T)\frac{dT}{T} - \int R_v \frac{dp}{p}, \tag{30}$$

given a functional form for $C_{p,v}(T)$, where it is required that s is null at 0 K. Therefore,

$$s_v = s_v^0 + \int_{T^0}^{T} C_{p,v}(T)\frac{dT}{T} - R_v \ln(p/p^0), \tag{31}$$

where s_v^0 is the reference entropy at the reference temperature T^0 and pressure p^0, typically obtained from integration or tables.

Considering the entire g contribution due to drop source terms

$$g_d = g_{\mathrm{III}} + g_{\mathrm{II}} + g_{\mathrm{I,kine}} + g_{\mathrm{I,chpot}}, \tag{32}$$

$$g_d = -\frac{Q_{\mathrm{conv\text{-}diff}}}{T} - \dot{m}_d s_{v,s} - \frac{\dot{m}_d}{T}\frac{u_{sl,i}u_{sl,i}}{2} + \frac{M_d}{\tau_d} f_1 \frac{u_{sl,i}u_{sl,i}}{T}, \tag{33}$$

having assumed that s_v is calculated at the drop surface (consistent with the calculation of h_v in S_{en}), shows that because the last term in Eq. (33) is always positive, the sign of g_d is determined by the sign and magnitude of the first three terms. By definition, under net evaporative conditions, $\dot{m}_d < 0$, and thus the second and third terms of Eq. (33) are also positive; the opposite happens under net condensation conditions. Finally, for $T_d < T$, which are the prevailing conditions in the present simulations, the first term is negative. Thus, under net evaporative conditions, the sign of g_d is determined by the relative magnitude of the first term compared to the sum of the other terms of Eq. (33). The implication is that strong droplet heating promoted by a large value of $(T - T_d)$ could lead to a reduction in g (with respect to a SP flow having the same thermodynamic gradients) if evaporation is weak, that is, if the liquid is not very volatile, and also if the slip velocity is small. These considerations show that liquid volatility plays a strong role in determining the value of the dissipation, and identifies the reasons why TP flows with liquids of different composition have disparate characteristics.

TABLE IV. Global entropy production for die375ML0R5, die375ML0R6, die375ML0R5X, and die375ML0R6X at t_{tr}^*. Units are $\mathrm{Wm^{-3}K^{-1}}$.

	die375ML0R5		die375ML0R6		die375ML0R5X		die375ML0R6X	
Term	Average	rms	Average	rms	Average	rms	Average	rms
g_{visc}	1178	2125	1141	2198	1230	2236	1307	2611
g_{temp}	12	31	10	26	11	29	11	28
g_{mass}	0	0	0	0	87	272	81	280
g	1190	2135	1151	2208	1328	2325	1399	2693

Presented in Table IV is the g budget at t_{tr}^* for all $\mathrm{ML}_0 = 0$ simulations. SP simulations in which there is a species mass flux (of similar magnitude to that occurring at transitional states for the MC TP flows) exhibit not only the additional g_{mass} contribution to g, but also a larger g_{visc} (both average and rms) compared to the equivalent SP simulations without species mass flux. Furthermore, with increasing Re_0, simulations having a species mass flux display about a factor of 2 larger increase in the g_{visc} rms than simulations devoid of species mass flux. For corresponding simulations, both g and its contributions are larger for SC SP flows (compare Table IV to Table 10 of Ref. 20), indicating that even for SP situations, the MC feature may affect the turbulent characteristics of a flow, mainly through the change in molar mass.

Because calculation of the g budget involves for TP flows the value of s_v^0, which may be difficult to compute for MC liquids, this potential intricacy is avoided here by considering the budget of

$$g^* = g - s_v^0 S_{\mathrm{mass}}, \tag{34}$$

which is the irreversible entropy production associated with $(s - s_v^0)$, and by calculating $(s - s_v^0)$ according to Eq. (31) with the choice of $T^0 = T_b$ so as to eliminate the computation of the problematic liquid entropy; we choose $p^0 = p_0$. The budget of g^* is calculated in the same manner as that of g, except that in Eq. (26), $g_{\mathrm{I,chpot}}$ is now replaced by $g_{\mathrm{I,chpot}}^* = g_{\mathrm{I,chpot}} - s_v^0 S_{\mathrm{mass}}$. The g^* budget for TP simulations at t_{tr}^* is presented in Tables V and VI for quantities calculated at grid nodes (e.g., the first row and first column value represents $\langle\langle g_{\mathrm{III}}\rangle\rangle$), and in Table VII for quantities calculated at grid nodes and

TABLE V. Volumetric entropy production for die375ML2R5, die375ML5R5, and die400ML2R5 at t_{tr}^{*}. Units are $Wm^{-3}K^{-1}$.

	die375ML2R5 Volumetric				die375ML5R5 Volumetric				die400ML2R5 Volumetric			
Term	Average	rms	%>0	%<0	Average	rms	%>0	%<0	Average	rms	%>0	%<0
g_{III}	7307	24695	57	17	16097	42372	70	9	8423	30536	55	22
$g_{\mathrm{I,chpot}}^{*}$	−11479	50145	28	47	−23045	89873	28	51	−12203	58544	29	46
g_{visc}	3296	7248	100	0	3479	7543	100	0	3314	7296	100	0
g_{II}	152	4612	37	38	575	9647	42	37	26	3767	35	39
g_{mass}	122	447	100	0	155	632	100	0	160	601	100	0
g_{temp}	138	426	100	0	176	599	100	0	240	731	100	0
$g_{\mathrm{I,kine}}$	30	232	47	28	71	365	51	28	27	281	46	29
g^{*}	−435	24917	78	22	−2492	45894	72	28	−14	27593	80	20

then interpolated at the drop location (e.g., the first row and first column value represents $\{\{g_{\mathrm{III}}^{\mathcal{I}}\}\}$, i.e., $g_{\mathrm{III}} \xrightarrow{\mathcal{I}} g_{\mathrm{III}}^{\mathcal{I}} \rightarrow \{\{g_{\mathrm{III}}^{\mathcal{I}}\}\}$). All tables list averages, rms, and the % of the ensemble where positive or negative values occur. The vertical listing of terms in the tables follows that of Ref. 20 (where they were listed in decreasing order of rms values for the baseline case) for easy comparison of terms other than $g_{\mathrm{I,chpot}}^{*}$ and g^{*}.

It is apparent from Table V that, excluding the noncomparable $g_{\mathrm{I,chpot}}^{*}$, the decreasing order of the rms values remains from the SC n-decane study of Ref. 20. However, at the same initial conditions, g_{III} is smaller in magnitude, whether average or rms, and this holds for diesel and all kerosenes (Tables V and VI), with RP-1, the liquid with the narrowest PDF, approaching n-decane most closely. For diesel at the (7% relatively) higher T_0 (Table V), g_{III} is larger by ~15% for the average and ~23% for the rms confirming the important influence of T_0 for liquids of low volatility. A similar comparison for Jet A (Table VI) reveals practically no variation with T_0, which is attributed to the more modest role of a such small relative increase in T_0 for fuels of higher volatility. Because

$$\begin{aligned}\mathrm{sign}(g_{\mathrm{III}}) &= -\,\mathrm{sign}\left[v_j F_j + Q_{\text{conv-diff}} + Q_{\text{evap}} + \dot{m}_d\left(\frac{v_j v_j}{2} + C_l T_d\right)\right] \\ &= -\,\mathrm{sign}\left[v_j F_j + \frac{\lambda Nu}{D}\frac{\ln(1+B_T)}{B_T}\pi D^2 (T - T_d) + \dot{m}_d\left(\frac{L_{v\mathrm{eff}}}{B} + \frac{v_j v_j}{2} + C_l T_d\right)\right] \end{aligned} \tag{35}$$

it is clear that $g_{\mathrm{III}}<0$ only if the sum of the first two terms, representing the work due to drag and drop heating, dominates the effect of evaporation. Although $\langle\langle g_{\mathrm{III}}\rangle\rangle>0$ for all simulations, and in most of the domain $g_{\mathrm{III}}>0$, there is a non-negligible % (more than 15%) of the volumetric domain where its value is negative for all $\mathrm{ML}_0=0.2$ simulations, and this percentage increases at the larger T_0. With increasing ML_0, the % of the domain with $g_{\mathrm{III}}<0$ decreases, which is attributed to the reduction in $\dot{m}_d$ combined with the larger drag and flow-to-drop heat transfer associated with the much larger number of drops. Of note, the percentages of strictly

TABLE VI. Volumetric entropy production for jetA375ML2R5, jetA400ML2R5, and rp1375ML2R5 at t_{tr}^{*}. Units are $Wm^{-3}K^{-1}$.

	jetA375ML2R5 Volumetric				jetA400ML2R5 Volumetric				rp1375ML2R5 Volumetric			
Term	Average	rms	%>0	%<0	Average	rms	%>0	%<0	Average	rms	%>0	%<0
g_{III}	10018	35523	58	18	10016	37759	56	19	12383	39873	61	15
$g_{\mathrm{I,chpot}}^{*}$	−15351	63611	25	51	−14524	64159	26	50	−19090	68136	19	57
g_{visc}	3288	7310	100	0	3228	7235	100	0	3373	7480	100	0
g_{II}	−6	3527	34	41	−95	2744	27	48	−28	3574	31	45
g_{mass}	201	770	100	0	254	942	100	0	197	745	100	0
g_{temp}	182	577	100	0	294	943	100	0	153	469	100	0
$g_{\mathrm{I,kine}}$	43	297	51	25	38	321	50	26	63	333	57	19
g^{*}	−1625	27387	77	23	−1625	27387	77	23	−2949	27565	72	28

TABLE VII. Drop-ensemble-based entropy production for die375ML2R5, die375ML5R5, and jetA375ML2R5 at t_{tr}^{*}. Units are $Wm^{-3}K^{-1}$.

	die375ML2R5 Drop-ensemble				die375ML5R5 Drop-ensemble				jetA375ML2R5 Drop-ensemble			
Term	Average	rms	%>0	%<0	Average	rms	%>0	%<0	Average	rms	%>0	%<0
g_{III}	27210	63584	64	36	42611	97944	82	18	38499	100234	63	37
$g_{I,chpot}^{*}$	−45172	134423	59	41	−59245	209757	60	40	−61279	184177	52	48
g_{visc}	2308	5808	100	0	2560	6961	100	0	2199	5589	100	0
g_{II}	190	12785	48	52	455	25300	52	48	−155	9413	48	52
g_{mass}	152	543	99	1	152	748	99	1	268	1045	99	1
g_{temp}	288	848	99	1	280	1156	99	1	385	1190	99	1
$g_{I,kine}$	99	542	41	59	134	635	40	60	143	731	48	52
g^{*}	−14926	66548	66	34	−13053	106403	71	29	−19939	79451	64	36

positive and strictly negative g_{III} activity do not necessarily add up to 100 because there may be no activity at all in the considerable part of the domain represented by the upper stream; in fact, only ~74% to 79% of the volume is prone to non-null g_{III} activity, and this percentage increases at larger ML_0 or T_0 but is not sensitive to liquid volatility.

For all fuels and under all conditions, $\langle\langle g_{I,chpot}^{*}\rangle\rangle < 0$ and dominates g^{*} in magnitude; similarly, the rms of $g_{I,chpot}^{*}$ is the largest among all contributions to g^{*}. This means that the composition of the fuel has a major impact on the $(s-s_v^0)$ production. Both the $g_{I,chpot}^{*}$ average and rms increase with ML_0, but slightly less than proportionally, and with T_0 or larger fuel volatility.

In contrast to g_{III}, the g_{visc} contribution, whether average or rms, is larger in magnitude here (by ~20%) than in Ref. 20, decisively explaining why the smallest scales in the energy spectra of Fig. 4 contain orders of magnitude less energy here than in the equivalent spectra of Ref. 20. None of the parameters considered here (ML_0, T_0 or liquid volatility) affect this conclusion, which seems to be entirely related to the MC aspect of the flow. Like for all other flux-related dissipation terms (i.e., g_{mass} and g_{temp}), the entire domain has a positive activity. Relative to the SP budget of Table IV, g_{visc} is now larger by ~35% in average and ~29% in rms. Although at first consideration this result may seem contradictory to the reduced energy in the small scales for SP flows evident in Figs. 4(c) and 4(d), the fact is that the initial energy in SP and TP flows is not the same (because of the additional energy due to the presence of drops) as shown in Fig. 4(b), and moreover the kinetic energy in TP flows first increases with time compared to the decrease experienced by SP flows [Fig. 5(a)], which brings the correct perspective to this result.

Previously analyzed in detail by Okong'o and Bellan[20] in their n-decane study, here $\langle\langle g_{II}\rangle\rangle > 0$ for diesel, but $\langle\langle g_{II}\rangle\rangle < 0$ for all kerosenes independent of T_0, indicating that for diesel it is drag that dominates, whereas for the kerosenes it is evaporation that governs the sign of this term. Confirming this interpretation, $\langle\langle g_{II}\rangle\rangle$ becomes increasingly positive at the larger ML_0 and substantially decreases with augmenting T_0; the same variation is apparent for the rms, portraying the increased (decreased) heterogeneity in the flow with increasing (decreasing) ML_0 (T_0). For diesel, an approximately similar % of the domain experiences positive or negative g_{II} activity, whereas for all kerosenes there is a larger % of negative activity regions. At the larger ML_0, the % of regions of positive activity increases, which results from the increased drag on a larger number of drops combined with the decreased evaporation due to heat-transfer limitations; at the larger T_0 the opposite holds, owing to the increased evaporation rate due to promoted heat transfer combined with the decreased drag on smaller drops.

Both g_{mass} and g_{temp} are for all liquids more than a factor of 50 smaller than the largest g contribution, and $g_{I,kine}$ is even smaller. Because

$$\mathrm{sign}(g_{I,kine}) = \mathrm{sign}\left(-\frac{d(\mathcal{N}\theta_l)}{dt}\right) \tag{36}$$

this means that regions of $g_{I,kine} > 0$ ($g_{I,kine} < 0$) correspond to net evaporation (net condensation). Apparently, independent of the liquid, ML_0 or T_0, net evaporation occurs in a larger % of the domain than net condensation. The kerosenes with a narrower composition PDF (i.e., RP-1 and JP-7) are particularly prone to net evaporation over a larger part of the domain due to the lack of much more volatile species than the mean that could have condensed on the drops. Similarly, the extent of net evaporation regions also becomes more preponderant with increasing ML_0, presumably due to the larger number of drops, which increases the portions of the domain populated by drops. The results show almost no sensitivity to T_0, however with increasing liquid volatility, $g_{I,kine}$ increases, consistent with the plots of Fig. 5(b).

Compared to MC SP simulations, the values of all flux contributions of g are larger for MC TP flows, whether average or rms; this is similar to the SC results of Ref. 20. However, one noteworthy distinguishing feature is that in going from SC to MC flows, $\langle\langle g_{visc}\rangle\rangle$ increases by only half as much from SP to TP situations, whereas the g_{visc} rms augmentation is a factor of 3 larger than for SC flows, suggesting that the MC-liquid phase change suppresses the increase in the average and introduces additional variability in g_{visc}.

Whereas Tables V and VI correspond to the dissipation

in an Eulerian framework, Table VII is an example of the gas dissipation g^* at t^*_{tr} as "seen" by the drops, that is, in a Lagrangian framework. In this Lagrangian framework, the % regions of positive activity added to the % of negative activity locations yields 100%. A small error is evident in the computed values for g_{mass} and g_{temp}, which, although adding to the expected 100%, show an unphysical 1% region of negative activity; the computation error is evidently due to the operation $\mathcal{I}$. Whereas $|\langle\langle g^*\rangle\rangle|$ increases with increasing ML_0 and decreases with increasing T_0 (Table V), $|\{\{(g^*)^{\mathcal{I}}\}\}|$ decreases with increasing ML_0 (Table VII) and varies erratically with the composition (not shown; it increases for diesel and JP-7 and decreases for Jet A and RP-1). The variation of $|\langle\langle g^*\rangle\rangle|$ with increasing fuel volatility, that is, with a smaller γ (see Table I), is nonmonotonic as a decrease is shown from Jet A to diesel (Tables V and VI), but an increase occurs from Jet A to RP-1 (Table VI); however, $|\{\{(g^*)^{\mathcal{I}}\}\}|$ increases monotonically with γ (not shown). Similar to $\langle\langle g^*\rangle\rangle$, the negative value of $\{\{(g^*)^{\mathcal{I}}\}\}$ represents the dominance of $g^*_{I,chpot}$, which is the only negative contribution. For all liquids (only diesel and Jet A shown) and for each specified simulation, over the drop ensemble g_{III} has a much larger value than over the volume, both average and rms; $g^*_{I,chpot}$ is in average larger in magnitude than volumetrically by a factor of ~2.5 to 4.5 for diesel and ~4 for kerosenes, and its rms is larger than volumetrically by a factor of ~2 to 3; g_{visc} is smaller both in average and rms for all liquids; g_{II} has a similar average value but a larger rms for diesel, and a much larger absolute value (by a factor of 26) and a much larger rms for Jet A (and both other kerosenes; not shown); for all liquids, g_{mass} and g_{temp} are 50% to a factor of 2 larger in average and rms when calculated over the drop ensemble; and independently of liquid, $\{\{g^{\mathcal{I}}_{I,kine}\}\}$ is larger by a factor of 2–3 than $\langle\langle g_{I,kine}\rangle\rangle$ with a larger % of $g^{\mathcal{I}}_{I,kine}$ allocated to negative values, corresponding to net condensation, and approximately a factor of 2 larger in rms. For all liquids, the T_0 variation of each contribution to $(g^*)^{\mathcal{I}}$ is consistent with that seen for the domain statistics. The general picture obtained when scrutinizing g^* over the drop ensemble is that although the general conclusions are similar to those obtained for the g^* statistics over the volumetric domain, the details may vary considerably. This raises the question of how the composition PDF, which according to (16) is a DGPDF for the vapor at the drop surface, evolves in mathematical form from the drop surface to the grid nodes. This question is addressed next.

E. Vapor-composition PDF representation

The dissipation discussion above raises the possibility that given the different "appearance" of the flow in the Eulerian or Lagrangian frameworks, the vapor-composition PDF, which is a DGPDF at drop locations, may not have the same mathematical form at grid nodes. Le Clercq and Bellan[15] interpreted their pretransitional simulations to mean that the vapor composition remained a DGPDF, an approximation that was justified by the relatively lower heterogeneity in composition relative to the present transitional results. Thus, here we explore the mathematical form of the vapor-composition PDF through the excess moments ξ'_{nv} of Eq. (4). That is, we compare the vapor-composition PDF, of which we only know the calculated first four moments computed as the solution of the gas-phase equations, with the SGPDF that has the same first two moments as the computed PDF; this composition PDF has so far an unknown mathematical form.

Figures 20(a) and 20(b) show $\langle\xi'_{3v}/\xi^{SGPDF}_{3v}\rangle$ and Figs. 20(c) and 20(d) display $\langle\xi'_{4v}/\xi^{SGPDF}_{4v}\rangle$. In all cases, both $\langle\xi'_{3v}/\xi^{SGPDF}_{3v}\rangle$ and $\langle\xi'_{4v}/\xi^{SGPDF}_{4v}\rangle$ are very small, $\sim O(10^{-3})$, and negative, although the fourth-order moment tends to have values larger by a factor of 5 than the corresponding third moments. The smallest magnitude of $\langle\xi'_{3v}/\xi^{SGPDF}_{3v}\rangle$ and $\langle\xi'_{4v}/\xi^{SGPDF}_{4v}\rangle$ is in the lower and upper streams, while the mixing layer hosts the largest values. The deviation from the SGPDF increases with decreasing ML_0 [Figs. 20(a) and 20(c)] and with increasing T_0 [Figs. 20(b) and 20(d)]; at more elevated Re_0, the region of larger departure shifts toward the upper stream, and the departure from the SGPDF is larger [Figs. 20(a) and 20(c)]. A smaller ML_0, larger T_0 or higher Re_0 promotes evaporation [as evidenced by $\{\{D^2\}\}_{ml}/\{\{D^2_0\}\}$ in Fig. 6(b)] and thus the release of species that potentially could condense and could contribute to the formation of a PDF different from the SGPDF. Notably, Harstad *et al.*[14] showed that for the liquid, departures from the SGPDF increased at larger evaporation rates and these departures were traced to species condensation on the drops. The departure from the SGPDF decreases in the lower stream with increasing value of the lowest-m species (Fig. 2), as vapor evolution in this region is entirely due to the most volatile species of the liquid. Because Jet A exhibits considerably more evaporation here than diesel and the two other kerosenes, its P_v displays the largest departure from the SGPDF [Figs. 20(b) and 20(d)]. The mixing layer being a region of evaporation where a multitude of molar mass species are released from the drops, the departures from the SGPDF align here with the width of $P_{l,0}$ because more species are available for condensation, and accordingly the vapor emanating from the liquid with the largest $P_{l,0}$ width—diesel—has the largest departure from the SGPDF.

Finally, $\{\varepsilon_l\}$ [see Eq. (1) for the definition of ε_l] is illustrated in Fig. 20(e) at t^*_{tr}, and now assuming that the vapor-composition PDF is of the double-Gamma form, $\langle\varepsilon_v\rangle$ is portrayed in Fig. 20(f) also at t^*_{tr}. The jagged aspect of the curves in Fig. 20(e) is due to ensemble averaging a liquid variable over drops residing in planes. The activity is almost uniquely confined to the mixing layer. Clearly, the deviation of the vapor composition from SGPDF is greater by ~50% in the vapor than in the liquid, although in both cases the departure is small; according to Harstad *et al.*,[14] however, this small departure is crucial to the physical tenability of the model. Thus, if P_v is a DGPDF, its departure from the equivalent SGPDF is larger than that of P_l from its corresponding SGPDF. Comparing all liquids according to their composition, a relatively larger departure from the SGPDF in the liquid leads to a relatively smaller departure for the vapor. We interpret this opposite variation as being the effect of condensation onto the drops, which depresses the minor double-Gamma peak in the vapor and increases it in the liquid. This

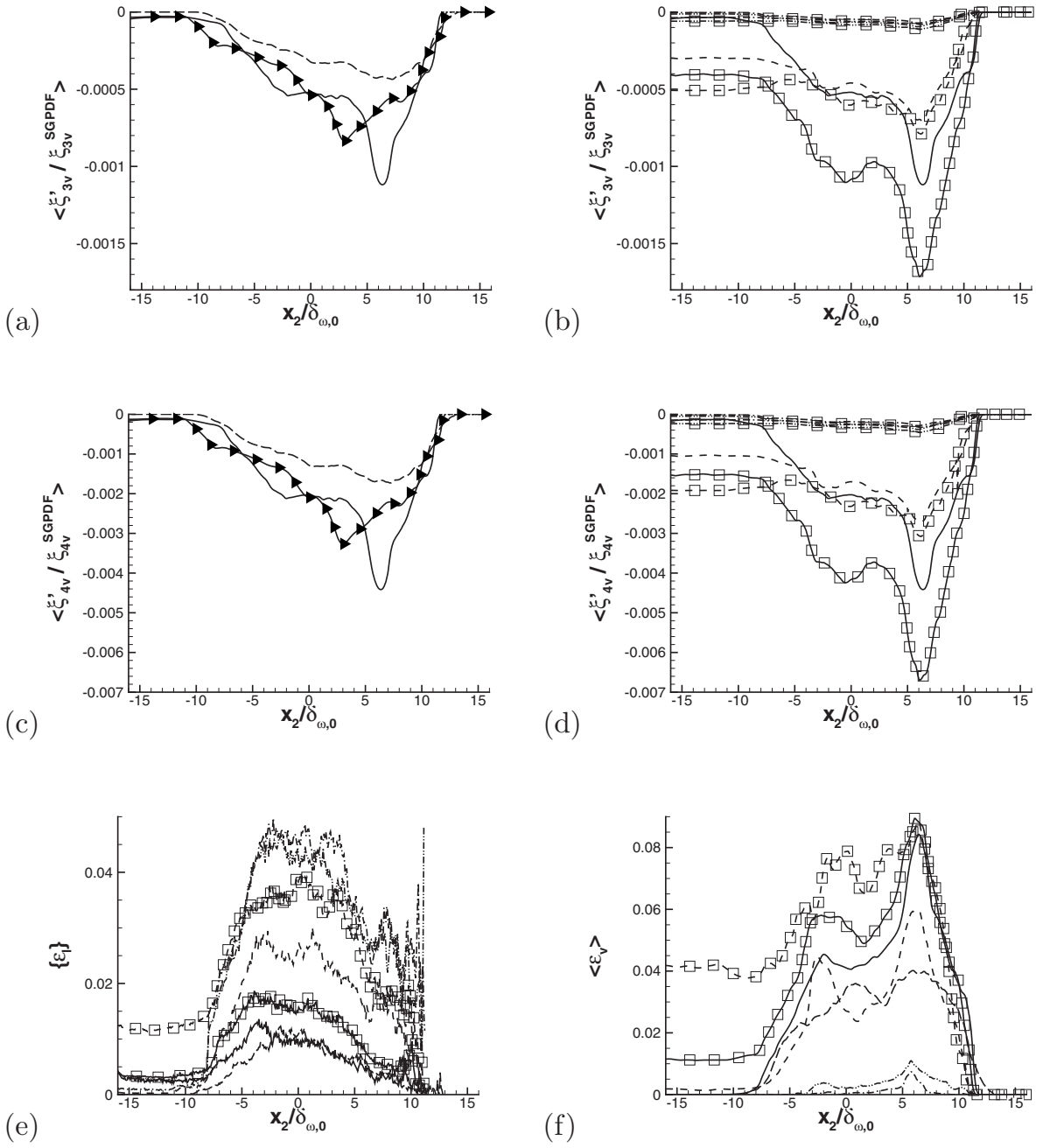

FIG. 20. Homogeneous (x_1, x_3) plane average vapor composition deviation at t^*_{tr} from the Gamma PDF: [(a) and (b)] $\langle \xi'_{3v} / \xi^{SGPDF}_{3v} \rangle$, [(c) and (d)] $\langle \xi'_{4v} / \xi^{SGPDF}_{4v} \rangle$, (e) $\{\varepsilon_l\}$, and (f) $\langle \varepsilon_v \rangle$. [(a) and (c)] die375ML2R2, die375ML2R5, and die375ML5R5; [(b) and (d)] die375ML2R5, die400ML2R5, jetA375ML2R5, jetA400ML2R5, rp1375ML2R5, rp1400ML2R5, jp7375ML2R5, and jp7400ML2R5; [(e) and (f)] die375ML2R5, die375ML5R5, die400ML2R5, jetA375ML2R5, jetA400ML2R5, rp1375ML2R5, and jp7375ML2R5. Curve labels are listed in the Figs. 3 and 5 captions, and die375ML2R2 —▶—.

interpretation is supported by the approximate coincidence of the peaks in Fig. 20(f) with the peaks in plots of homogeneous (x_1, x_3) plane average vapor composition at t^*_{tr} for both mean and standard deviation (Fig. 19). The largest deviation in the liquid and the least departure in the vapor from the SGPDF are for RP-1 and JP-7 because of their narrower initial composition PDF, implying a narrower range of saturation pressures. Decreasing (increasing) in deviation from SGPDF, Jet A liquid (vapor) is intermediary between the other two kerosenes and diesel. At the more elevated T_0 (ML_0), both liquid and vapor experience larger (smaller) DGPDF effects. The major and minor mixing-layer peaks in Fig. 20(f) coincide with isolated regions of high drop number density (Fig. 8), prone to large net evaporation.

V. SUMMARY AND CONCLUSIONS

Transitional states were created through Direct Numerical Simulation (DNS) for both multicomponent-species (MC-species) gaseous mixing layers and drop-laden mixing layers where the evaporating liquid is a MC mixture of a very large number of species. The mixing layer was three-dimensional, and when drops were present, they were initially confined to the lower stream. The gas was followed in

an Eulerian framework, whereas the drops were described in a Lagrangian frame, with complete dynamic and thermodynamic coupling between drops and carrier gas. The liquid and vapor composition resulting from evaporation/condensation was modeled using Continuous Thermodynamic concepts wherein a Probability Distribution Function (PDF), taken here as a function of the species molar mass, describes each evolving PDF; the gas PDF is a function of time and location, and the liquid PDF varies with time and is specific to each drop. The liquid PDF was initially specified as a single Gamma PDF (SGPDF) and was allowed to evolve into a linear combination of two Gamma PDFs (DGPDF).

For gaseous [i.e., single-phase (SP)] mixing layers, the emphasis was on the characteristics of the transitional states as a function of the initial Reynolds number and of the initial species mass flux between the two streams. For drop-laden [i.e., two-phase (TP)] mixing layers, the emphasis was on the drop/flow interaction, the influence of the initial mass loading the impact of the initial carrier gas temperature and the effect of the identity of the liquid.

Our conclusions are threefold: first the scrutiny of the present MC-liquid transitional simulations allowed the sorting of features influenced or not by the initial composition of the liquid; then, comparisons of the present findings with the pretransitional DNS solutions of Le Clercq and Bellan[15] using the same model as here revealed the impact of small-scale activity; finally, comparisons with the single-component (SC) DNS results of Okong'o and Bellan[20] were also performed to differentiate MC and SC liquids.

Analysis of the present database revealed that the identity of the liquid has a minor influence on the global features of the flow such as momentum thickness, positive spanwise vorticity, enstrophy, and even energy spectra. It is thus clear that these quantities are poor candidates as tests for model validation using experimental results. Quantities such as droplet temperature and composition or the amount of vapor released and its composition proved to be very sensitive to the nature of the liquid. It was found that not only the initial mean molar mass of the liquid has an impact on the vapor composition evolution, but also the variety of species initially present, that is, the width of the initial PDF. In particular, the total mass of vapor proved to be strongly correlated with the mean of the composition PDF, whereas the vapor composition was more sensitive to the liquid-PDF width.

Comparison with the pretransitional database of Le Clercq and Bellan[15] showed that the influence of the Reynolds number is mostly in the generation of more local heterogeneity rather that in drastic changes in global quantities. For example, unlike the results of Le Clercq and Bellan,[15] regions of high gas mean molar mass no longer entirely coincided with regions of high vapor composition standard deviation, which is attributed to the enhanced mixing and droplet dispersion due to turbulence.

Using the results of Okong'o and Bellan,[20] it was found that the global evolution of the layer was hardly affected by the nature of the liquid (i.e., SC versus MC), again giving strong indications toward useful diagnostics for experimental validation of the models. However, it was also found that with otherwise identical initial conditions, the energy spectra of MC-liquid and SC-liquid laden mixing layers are different. The discrepancy occurs at the smallest scales where MC flows have much less energy than their SC counterpart. The assessment of the dissipation balance at transition showed that the viscous dissipation here is indeed larger by approximately 20% for diesel (the exact amount is liquid composition dependent) than for the n-decane simulations of Ref. 20, explaining the reduced energy in the smallest scales. For SP flows, it was found that both the total dissipation and each of its contributions were smaller for MC flows than in corresponding SC simulations. Therefore, whether gaseous or drop-laden flows, the gas composition has an impact on the turbulent characteristics of the flow. Thus, the indication is that discriminating measurements between SC and MC flows, which are so far unavailable, could initially focus on dissipation aspects. The difference in small-scale behavior between MC and SC cases at otherwise similar flow initial conditions suggests that SGS models in LES may have different importance in portraying the flow; this is a subject for further investigation.

To summarize, transitional MC flows display significant distinctive features from transitional SC flows having the same initial conditions. Not only are there strong vapor and (if applicable) liquid composition nonuniformities in the layer, but also the turbulent character of the flow is different. The conclusion is that neither experiments nor theory conducted with SC flows are good surrogates for a MC flow application. As in pretransitional simulations, composition effects are amplified with increasing carrier gas temperature, but here additionally the initial carrier gas temperature has a significant impact on the highest local magnitude of the vorticity. Whereas in pretransitional MC TP flows the regions of high-molar-mass vapor species entirely coincided with those of high vapor-PDF standard deviation, this is no longer the case.

The next stage of this study will be devoted to *a priori* and *a posteriori* investigations, so as to reduce the large computational time of DNS and replace DNS with computationally efficient large eddy simulations, akin to the studies of Leboissetier *et al.*[41] Currently, there are no data available for MC model validation. The diagnostics for producing experimental data for model validation are still in their infancy.[42] The present investigation highlighted the experimental measurements that would be necessary for meaningful comparisons with simulations. Such data should preferably contain all, or at least some, of the following quantities: drops size and composition, vapor composition and drop field visualizations at different initial gas temperatures, Reynolds numbers, and mass loadings.

ACKNOWLEDGMENTS

This study was conducted at the Jet Propulsion Laboratory (JPL), California Institute of Technology (Caltech), under the partial sponsorship of the Donors of The Petroleum Research Fund administered by the American Chemical Society through a grant (to J.B.) for Caltech Post Doctoral Fellow support and the U.S. Department of Energy under an agreement with the National Aeronautics and Space Admin-

istration. The authors wish to thank Dr. Kenneth G. Harstad of JPL for useful discussions. Computational resources were provided by the supercomputing facility at JPL.

APPENDIX: CALCULATION OF THE HEAT FLUX PORTION DUE TO TRANSPORT OF MOLAR FLUXES

Details of the heat flux in Eq. (7) are as follows:

$$\alpha_1(T) = R_u A_p (A_b - T) - \Delta s_{lg} A_b, \tag{A1}$$

$$\alpha_2(T) = (C_{p,a} - R_u B_p) T + R_u (A_b B_p + A_c B_b) - \Delta s_{lg} B_b - C_l A_b, \tag{A2}$$

$$\alpha_3 = B_b [R_u B_p - C_l], \tag{A3}$$

where $C_{p,a} = \gamma_{ther,a} R_u / (\gamma_{ther,a} - 1) m_a$ [kJ/(kg K)] is the air heat capacity at constant pressure, $m_a = 29$ kg/kmol, $\gamma_{ther,a} = 1.4$ is the ratio of gas heat capacities, $\Delta s_{lg} = m L_v / T_b$, where L_v is the latent heat and T_b is the normal boiling point, $R_u = 8.3142$ [kJ/(kmol K)] and

$$C_p(m) = (A_p + B_p m) R_u / m \quad \text{in [kJ/(kgK)]} \tag{A4}$$

is the gas heat capacity where $A_p = 2.465 - 1.144 \times 10^{-2} T_r + 1.759 \times 10^{-5} T_r^2 - 5.972 \times 10^{-9} T_r^3$ and $B_p = -0.03561 + 9.367 \times 10^{-4} T_r - 6.030 \times 10^{-7} T_r^2 + 1.324 \times 10^{-10} T_r^3$ (see Chou and Prausnitz[4]) with the reference temperature T_r being that of Miller *et al.*[27] Following Tamim and Hallett,[7] $C_l = 2.26 - 2.94 \times 10^{-3} T_{r,d} + 9.46 \times 10^{-6} T_{r,d}^2$ (kJ/kg K), where $T_{r,d} = T_r$. Constants A_b and B_b are given in Sec. II B.

More details and transport property values are given in Appendix A of Le Clercq and Bellan.[15]

[1] R. B. Landis and A. F. Mills, "Effect of internal diffusional resistance on the evaporation of binary droplets," 5th International Heat Transfer Conference, Tokyo (1974), Vol. 4, p. 345.

[2] R. L. Cotterman, R. Bender, and J. M. Prausnitz, "Phase equilibria for mixtures containing very many components. Development and application of continuous thermodynamics for chemical process design," Ind. Eng. Chem. Process Des. Dev. **24**, 194 (1985).

[3] B. Gal-Or, H. T. Cullinan, Jr., and R. Galli, "New thermodynamic-transport theory for systems with continuous component density distributions," Chem. Eng. Sci. **30**, 1085 (1975).

[4] G. F. Chou and J. M. Prausnitz, "Adiabatic flash calculations for continuous or semicontinuous mixtures using an equation of state," Fluid Phase Equilib. **30**, 75 (1986).

[5] M. T. Rätzsch and H. Kehlen, "Continuous thermodynamics model of complex mixtures," Fluid Phase Equilib. **14**, 225 (1983).

[6] C. H. Whitson, "Characterizing hydrocarbon plus fractions," SPEJ **23**, 683 (1983).

[7] J. Tamim and W. L. H. Hallett, "A continuous thermodynamics model for multicomponent droplet vaporization," Chem. Eng. Sci. **50**, 2933 (1995).

[8] W. L. H. Hallett, "A simple model for the vaporization of droplets with large numbers of components," Combust. Flame **121**, 334 (2000).

[9] A. M. Lippert and R. D. Reitz, "Modeling of multicomponent fuels using continuous distributions with application to droplet evaporation and sprays," SAE Paper 97FL-468 (1997).

[10] P. C. Le Clercq and J. Bellan, "Direct numerical simulation of a transitional temporal mixing layer laden with multicomponent-fuel evaporating drops using continuous thermodynamics," Phys. Fluids **16**, 1884 (2004).

[11] K. Harstad, "Trend analysis for atmospheric hydrocarbon partitioning using continuous thermodynamics," J. Atmos. Sci. **62**, 2977 (2005)

[12] M. Arias-Zugasti and D. E. Rosner, "Multicomponent fuel droplet vaporization and combustion using spectral theory for a continuous mixture," Combust. Flame **135**, 271 (2003).

[13] K. Harstad and J. Bellan, "Modeling evaporation of Jet A, JP-7 and RP-1 drops at 1 to 15 bars," Combust. Flame **137**, 163 (2004).

[14] K. G. Harstad, P. C. Le Clercq, and J. Bellan, "A statistical model of multicomponent-fuel drop evaporation for many-droplet gas-liquid flow simulations," AIAA J. **41**, 1858 (2003).

[15] P. C. Le Clercq and J. Bellan, "Direct numerical simulation of gaseous mixing layers laden with multicomponent-liquid drops: Liquid-specific effects," J. Fluid Mech. **533**, 57, (2005).

[16] M. Boivin, S. Simonin, and K. D. Squires, "Direct numerical simulation of turbulence modulation by particles in isotropic turbulence," J. Fluid Mech. **375**, 235 (1988).

[17] F. Mashayek, "Droplet-turbulence interactions in low-Mach-number homogeneous shear two-phase flows," J. Fluid Mech. **367**, 163 (1998).

[18] F. Mashayek, "Direct numerical simulations of evaporating droplet dispersion in forced low-Mach-number turbulence," Int. J. Heat Mass Transfer **41**, 2601 (1998).

[19] F. Mashayek and F. A. Jaberi, "Particle dispersion in forced isotropic low-Mach-number turbulence," Int. J. Heat Mass Transfer **42**, 2823 (1999).

[20] N. A. Okong'o and J. Bellan, "Consistent large eddy simulation of a temporal mixing layer laden with evaporating drops. Part I: Direct numerical simulation, formulation and *a priori* analysis," J. Fluid Mech. **499**, 1 (2004).

[21] J. Réveillon and L. Vervisch, "Spray vaporization in nonpremixed turbulent combustion modeling: A single drop model," Combust. Flame **121**, 75 (2000).

[22] F. A. Williams, *Combustion Theory* (Addison-Wesley, Reading, MA, 1965).

[23] R. S. Miller and J. Bellan, "Direct numerical simulation of a confined three-dimensional gas mixing layer with one evaporating hydrocarbon-droplet laden stream," J. Fluid Mech. **384**, 293 (1999).

[24] K. G. Harstad and J. Bellan, "Modeling of multicomponent homogeneous nucleation utilizing continuous thermodynamics," Combust. Flame **139**, 252 (2004).

[25] R. S. Miller and J. Bellan, "Direct numerical simulation and subgrid analysis of a transitional droplet laden mixing layer," Phys. Fluids **12**, 650 (2000).

[26] R. D. Moser and M. M. Rogers, "Mixing transition and the cascade to small scales in a plane mixing layer," Phys. Fluids A **3**, 1128 (1991).

[27] R. S. Miller, K. Harstad, and J. Bellan, "Evaluation of equilibrium and non-equilibrium evaporation models for many-droplet gas-liquid flow simulations," Int. J. Multiphase Flow **24**, 1025 (1998).

[28] G. K. Batchelor, *The Theory of Homogeneous Turbulence* (Cambridge University Press, Cambridge, UK, 1967).

[29] T. Edwards and L. Q. Maurice, "Surrogate mixtures to represent complex aviation and rocket fuels," J. Propul. Power **17**, 461 (2001).

[30] T. Edwards (private communication).

[31] M. Baum, T. J. Poinsot, and S. K. Lele, "Accurate boundary conditions for multicomponent reactive flows," J. Comput. Phys. **116**, 247 (1994).

[32] T. J. Poinsot and S. K. Lele, "Boundary conditions for direct simulations of compressible viscous flows," J. Comput. Phys. **101**, 104 (1992).

[33] C. Kennedy and M. Carpenter, "Several new numerical methods for compressible shear layer simulations," Appl. Numer. Math. **14**, 397 (1994).

[34] H. Tennekes and J. L. Lumley, *A First Course in Turbulence* (MIT Press, Cambridge, MA, 1972).

[35] A. J. Chorin, *Vorticity and Turbulence*, Applied Mathematics Science Vol. 103 (Springer, Berlin, 1991).

[36] A. W. Vreman, "Turbulence characteristics of particle-laden pipe flow," J. Fluid Mech. **584**, 235 (2007).

[37] K. D. Squires and J. K. Eaton, "Preferential concentration of particles by turbulence," Phys. Fluids A **3**, 1169 (1991).

[38] H. L. Goldstein and C. W. Siegmund, "Influence of heavy fuel oil composition and boiler combustion conditions on particulate emissions," Environ. Sci. Technol. **10**, 1109 (1976).

[39] H. Groenzin and O. C. Mullins, "Molecular size and structure of asphaltenes from various sources," Energy Fuels **14**, 677 (2000).

[40] E. Y. Sheu, "Petroleum asphaltene—Properties, characterization, and issues," Energy Fuels **16**, 74 (2002).

[41] A. Leboissetier, N. A. Okong'o, and J. Bellan, "Consistent large eddy simulation of a temporal mixing layer laden with evaporating drops. Part 2: *A posteriori* modeling," J. Fluid Mech. **523**, 37 (2005).

[42] Y. Zhao and H. H. Qiu, "Measurements of multicomponent microdroplet evaporation by using Rainbow Refractometer and PDA," Exp. Fluids **40**, 60 (2006).